Innate immune sensing of self-derived double-stranded RNA by RIG-I-MAVS-TNF-α regulates the survival and senescence fate of SARS-2-S syncytia

Luming Wan[1*], Huilong Li[1,2*], Linfei Huang[1*], Muyi Liu[1*], Jingfei Li[1*], Yilong Yang[1*], Ruzhou Zhao[1], Jialong Liu[1], Xiaopan Yang[1], Enhao Ma[3], Lijuan Sun[4], Xufeng Hou[4], Xuhui Zhang[4], Yanhong Zhang[1], Qiulin Yan[1], Jing Liu[4], Xinyu Li[1], Gong Cheng[3], Qi Gao[4,5], Junjie Xu[1,5], Lihua Hou[1,2,5], Congwen Wei[1,5], and Hui Zhong[1,5] ✉

[1]Beijing Institute of Biotechnology, Beijing, China.

[2]College of Basic Medical Sciences, School of Medicine, Zhejiang University, Hangzhou, China.

[3] Tsinghua-Peking Center for Life Sciences, School of Medicine, Tsinghua University, Beijing, China.

[4]Beijing Glyexo Gene Technology Co. Ltd., Beijing, China.

[5]These authors jointly supervised the work: Qi Gao, Junjie Xu, Lihua Hou, Congwen Wei, and Hui Zhong

✉ Lead Correspondence: Hui Zhong, towall@yahoo.com

[*]These authors contributed equally to this work: Luming Wan, Huilong Li, Linfei Huang, Muyi Liu, Jingfei Li, and Yilong Yang

Running Title: The RIG-I-MAVS-TNF-α axis regulates the fate of SARS-2-S syncytia

Abstract

The coronavirus disease 2019 (COVID-19) pandemic caused by severe acute respiratory syndrome coronavirus 2 (SARS-CoV-2) remains an important health threat. Syncytial formation by infected cells mediated by the SARS-CoV-2 spike protein (SARS-2-S) is a hallmark of COVID-19–associated pathology. Although SARS-CoV-2 infection evokes cellular senescence, as in other viruses, the direct link between SARS-2-S-induced syncytia with senescence in the absence of viral infection and their senescence fate determinants remain unknown. Here, we show that syncytia formed by cells expressing exogenously delivered SARS-2-S exhibited a senescence-like phenotype *in vitro* and that SARS-2-S mRNA induced senescence phenotype *in vivo*. Extracellular vesicles (EVs) containing SARS-2-S also induced senescent syncytium formation independent of the *de novo* synthesis of SARS-2-S. Mechanistically, we show that the accumulation of endogenous dsRNA, partially that whose formation is induced by activation of the unfolded protein response (UPR), in SARS-2-S syncytia triggers RIG-I-MAVS signalling to drive the TNF-α-dependent survival and senescence fate of SARS-2-S syncytia. Our findings suggest that the fusogenic ability of SARS-2-S might contribute to the side effects of particular COVID-19 vaccines or perhaps long COVID-19 syndrome and provide insight into how these effects can be prevented.

Main text

Coronavirus disease 2019 (COVID-19), which is caused by severe acute respiratory syndrome coronavirus 2 (SARS-CoV-2), has resulted in a global pandemic, with 608 million confirmed infections and 6.5 million deaths as of September 2022[1]. Extensive alveolar damage, the presence of massive lung thrombosis, and the common presence of syncytial pneumocytes constitute three hallmarks of critical SARS-CoV-2 infection[2, 3]. Syncytium formation represents one important mechanism behind the pathogenicity of SARS-CoV-2 infection, by either disseminating the virus or triggering inflammatory immune responses[4-8].

Syncytium formation is mediated by the SARS-CoV-2 spike protein (SARS-2-S)[5]. SARS-2-S interacts with the ACE2 receptor on the host cell and is then proteolytically activated by host proteases, leading to cell–cell fusion[9]. The presence of SARS-2-S on the cell surface is sufficient to mediate the merging of cell membranes expressing ACE2, a mechanism called fusion from within (FFWI)[10]. The fusogenic activity of SARS-2-S is potent, as even undetectable amounts of SARS-2-S can cause cell–cell fusion[10]. In addition to mediating FFWI, virus-like particles or lipid vesicles containing surface SARS-2-S can serve as a bridge between two cells and induce fusion from without (FFWO)[10]. As a main antigenic determinant, SARS-2-S was used as the antigen in the majority of available COVID-19 vaccines, including the vaccines from AstraZeneca, Janssen, Pfizer/BioNTech's BNT162b2, and Moderna's mRNA-1273[11-13]. Full-length SARS-2-S is expressed as a foreign antigen on the surface of cells infected with adenovirus or transfected with mRNA. Similar to other proteins produced by the body,

the spike proteins generated by COVID-19 vaccines last up to a few weeks[14]. Notably, BNT162b2 vaccination produces EVs carrying SARS-2-S (S-EVs) on day 14 following the first dose of vaccination that last for several months, and the amount of S-EVs increases up to 12-fold after the second booster dose of the vaccine[15]. With its high fusogenic efficiency and persistence, it is thus reasonable to presume that SARS-2-S in vaccine-injected individuals may have a great chance of inducing syncytial formation via both FFWI and FFWO mechanisms. Cell–cell fusion in uninfected cells may also occur in long COVID-19 syndrome, as spike protein fragments were detected in blood samples from long COVID-19 patients who suffered up to a year after their original infection[16]. Although much is known about the SARS-2-S protein, the implication of the fusogenic property of SARS-2-S in vaccine side effects and long COVID-19 complications is still largely unknown.

SARS-CoV-2 elicits the senescence of infected cells[17]. Cellular senescence is a state of stable cell cycle arrest characterized by increased lysosomal activity, exemplified by induction of the lysosomal enzyme senescence-associated β-galactosidase (SA-β-gal) and activation of the senescence-associated secretory phenotype (SASP)[18]. SARS-CoV-2 infection triggers paracrine senescence and can lead to a hyperinflammatory environment and the onset of acute respiratory disease syndrome[19]. Such senescence induction is not restricted to SARS-CoV-2 infection, as multiple viruses have been reported to activate senescence responses[20]. While the importance of activation of the DNA damage response in promoting paracrine senescence and the production of the SASP by SARS-CoV-2 infection or the SARS-2-S protein has been indicated, the direct

link between the fusogenic property of SARS-2-S with senescence and its regulation is still unknown.

Here, we explored the biological properties and fate determinants of SARS-2-S syncytia. We show that SARS-2-S syncytia are senescent and that the senescent phenotype is an outcome of the recognition of self-derived dsRNA, generated by the activated unfolded protein response (UPR), by the RIG-I–MAVS pathway. Together, our findings may provide explanations for some complications caused by cell fusion specific to particular vaccines, deepen our understanding of the pathophysiology of COVID-19 and reveal new targets for intervention.

SARS-2-S-expressing syncytia exhibit a senescence-like phenotype

A distinctive feature of SARS-2-S is its ability to mediate the merging of cell membranes expressing ACE2, with the ensuing formation of giant multinucleated cells (syncytia). In the current study, we first tested the kinetics of syncytium formation by A549 cells. When we cocultured SARS-2-S (Wuhan-Hu-1)-expressing A549 cells with ACE2-expressing A549 cells at a 1:1 ratio (Extended Data Fig. 1a–c), syncytial cells rapidly appeared at 4 h post-coculture (hpc) and gradually grew in size, as indicated by microscopic analysis (Fig. 1a). Notably, SARS-2-S-expressing syncytia (hereafter referred to as SARS-2-S syncytia) with enhanced SA-β-gal staining began to appear at 12 hpc, and the percentage of SA-β-gal-positive syncytia among SARS-2-S syncytia gradually increased during the fusion process (Fig. 1a). We did not observe multinucleated cells or SA-β-gal–positive staining in A549 cells that only expressed SARS-2-S or ACE2 at the time points tested (Extended Data Fig. 1d). Quantitative real-time PCR (RT-qPCR) revealed significant transcriptional upregulation of senescence-associated genes (Fig. 1b and Extended Data Fig. 1e). Consistently, the conditioned medium of SARS-2-S syncytia at 48 hpc contained significantly more SASP-related cytokines, such as TNF-α, IL-6, IL-8, and IL-2, than that at 0 hpc (Fig. 1c). Notably, the appearance of SA-β-gal positive staining was associated with syncytial nuclei number. Eventually, over 70% of SARS-CoV-2-S syncytia exhibited positive SA-β-gal staining at 72 hpc (Fig. 1d). In a similar manner, we observed SARS-2-S–induced senescence during coculture of the same and different cell types (Fig. 1e). In contrast to wild-type SARS-2-S, a SARS-2-SNF mutant (R682A R683A R685A K814A

R815A), which fails to cause fusion because it cannot be cleaved by host protease, lost the ability to induce senescence[21, 22] (Fig. 1f and Extended Data Fig. 1f). We next compared the senescence potential of the Omicron variant (SARS-2-SO) with that of SARS-2-S (Extended Data Fig. 1f). As reported, the Omicron S protein showed weaker fusogenic activity than SARS-2-S[23] (Fig. 1f, g). Notably, while the SARS-2-SO syncytia were much smaller and had fewer nuclei than those formed by SARS-2-S, the percentage of SA-β-gal-positive syncytia was comparable to that of SARS-2-S, although they formed more slowly (Fig. 1f and Extended Data Fig. 1g). Furthermore, SARS-2-S syncytia could be selectively killed by senolytic drugs, including the multiple-kinase inhibitor Fisetin, the tyrosine kinase inhibitor Dasatinib, and the BCL-2–specific Venetoclax (Fig. 1h, i, j). Taken together, the above observations indicate that the SARS-2-S protein elicits a senescence-like phenotype that is dependent on syncytium formation *in vitro*.

SARS-2-S delivery by EVs or mRNA triggers syncytial senescence

Since BNT162b2 vaccination could induce the production of EVs carrying SARS-2-S (S-EVs), we then asked whether S-EVs have the ability to trigger syncytium formation and cell senescence in FFWI manner[15]. To this end, we first used ultracentrifugation to purify EVs from the supernatant of HeLa or SARS-2-S expressing HeLa cells, and confirmed their identity by probing for the exosome markers (Extended Data Fig. 2a, b). We next labelled these EVs with the fluorescent dye DiO and exposed A549 cells to the EVs and the expression of SARS-2-S on the surface of the cells that took up the S-EVs was observed (Extended Data Fig. 2c, d). These cells fused with cells expressing

ACE2 at 8 hpc, as indicated by the appearance of multinucleated cells (Fig. 2a). Importantly, the fused cells exhibited enhanced SA-β-gal and p21 staining, with a flattened and enlarged morphology and increased transcription of the *TNF*, *IL6*, *IL8*, and *CDKN1A* genes (Fig. 2a, b), features that are typical of senescence. We also noted the senescence phenotype in other similarly treated cell types but not in cells that took up EVs lacking SARS-2-S (Extended Data Fig. 2e, f). In addition, A549-ACE2 cells were incubated with S-EVs for 2 to 24 h, a timeframe in which *de novo* synthesis of SARS-2-S does not occur, to induce cell FFWO. Notably, S-EVs induced FFWO syncytium formation as early as 2 h and the appearance of senescent syncytia began to occur at 12 h (Fig. 2c, d). Eventually, about 70% of syncytia exhibited positive SA-β-gal staining at 48 h upon S-EVs addition (Fig. 2c).

We next asked if SARS-2-S delivered in the form of encoding mRNA to reflect an mRNA vaccine would also trigger syncytium formation and cell senescence. To this end, we packaged the encoding mRNA into a lipid nanoparticle formulation (S-mRNA-LNP). Western blotting confirmed the expression of SARS-2-S treated with S-mRNA-LNP (Extended Data Fig. 3b). Next, we cocultured S-mRNA-LNP–treated A549 cells with A549-ACE2 cells at a 1:1 ratio. Notably, syncytial cells formed rapidly and began to stain positive for SA-β-gal and p21 at 8 hpc (Fig. 2e). Significant upregulation of senescence-associated genes supported the presence of a senescence phenotype (Fig. 2f). We obtained similar results using 293T-ACE2 cells, but did not observe any signs of senescence in LNP- or S-mRNA-LNP-treated A549 (Extended Data Fig. 3c, d, e). This finding indicates that SARS-2-S has the ability to trigger syncytial senescence

regardless of its manner of delivery.

Finally, we explored whether cell senescence related to SARS-2-S-mediated cell fusion would also occur *in vivo*. To this end, we injected AAV-hACE2 constructs into the tail veins of 8-week-old C57BL/6 mice to drive mainly hepatic hACE2 expression (Extended Data Fig. 3f, g). Four weeks later, we intramuscularly (i.m.) administered a single dose of S-mRNA-LNP or LNP to the hACE2-expressing mice and examined the induction of senescence. Immunohistochemical analysis revealed robust SARS-2-S expression and the increased appearance of multinucleated cells with at least four nuclei in the livers of S-mRNA-LNP-treated mice compared to the livers of LNP-treated mice (Extended Data Fig. 3h and Fig. 2g). RNA sequencing (RNA-seq) of liver samples revealed the upregulated expression of cellular senescence-related genes (Fig. 2h). KEGG pathway analysis of differentially expressed genes (DEGs) revealed the enrichment of mainly antigen processing and presentation, fluid shear stress and atherosclerosis, the complement and coagulation cascades, and cellular senescence pathways (Extended Data Fig. 4). Finally, multiplex protein analysis of serum samples from these animals revealed that S-mRNA-LNP strongly induced SASP-reminiscent cytokines (Fig. 2i). We therefore concluded that SARS-2-S elicits features of senescence both *in vitro* and *in vivo*.

SARS-2-S syncytia provoke the RIG-I-dependent formation of functional MAVS aggregates

Cell fusion in the absence of SARS-CoV-2 infection activates the cGAS-STING pathway, which has been suggested to promote cellular senescence[8]. However, the

occurrence of senescence in SARS-2-S syncytia formed by HEK293T (hereafter referred to as 293T) cells lacking STING expression[24] indicated the existence of other signalling pathways that regulate SARS-2-S syncytial senescence. We then focused on mitochondrial antiviral signalling adaptor protein (MAVS), a mitochondrial adaptor protein that links the cytoplasmic RNA sensor RIG-I to its downstream signalling molecules by forming well-ordered prion-like aggregates[25]. As reported, the MAVS staining pattern became noticeably speckled in response to vesicular stomatitis virus (VSV) infection[26](Fig. 3a). Strikingly, MAVS was also redistributed as early as 3 hpc in SARS-2-S syncytia in a manner similar to its distribution in mitochondria (Fig. 3a and Extended Data Fig. 5a). Furthermore, MAVS aggregation during cell fusion proceeded in a manner similar to that induced by VSV infection, as determined by semi-denaturing detergent agarose gel electrophoresis (SDD-AGE) (Fig. 3b). While VSV infection began to trigger massive mitochondrial elongation and tubularization at 6 h post infection (hpi), we observed enhanced speckled staining of the mitochondria in SARS-2-S syncytia, with relatively less mitochondrial fusion, during the entire fusion process (Fig. 3a). Importantly, MAVS aggregation was reduced by knockdown of *Mitofusin* 1 (*MFN1*) but not by knockdown of *OPA1*; both of these proteins are mitochondrial membrane proteins that regulate mitochondrial dynamics and RIG-I-induced antiviral signalling[27] (Fig. 3c and Extended Data Fig. 5b). Accordingly, we knocked down the *RIG-I* gene (Extended Data Fig. 5b). We found that this significantly reduced MAVS aggregation in cocultured cells (Fig. 3d). MAVS aggregation in cocultured cells was also reduced by *MDA5* silencing, but this effect was much less

pronounced than that observed upon *RIG-I* silencing, though the knockdown efficiency was approximately 70% for both genes (Fig. 3d and Extended Data Fig. 5b). These data suggest the involvement of RIG-I, the primary sensor of nonself-derived dsRNA, in functional MAVS aggregation in SARS-2-S syncytia.

To confirm the spatiotemporal events linking RIG-I and MAVS during fusion, we performed a kinetic analysis of MAVS-RIG-I complex formation during cell fusion. Following the immunoprecipitation of endogenous MAVS, we detected increased levels of the RIG-I, TRAF3, and TRAF6 proteins in the immunoprecipitates as early as 4 hpc (Fig. 3e). In particular, the fusion process was accompanied by the increased phosphorylation levels of p65, IRF3, and TBK1, a measure of IFN-I signalling activity (Fig. 3f). Finally, the activity of the NF-κB promoter was dramatically enhanced in cocultured cells (Extended Data Fig. 5c). The above observations indicate the activation of RIG-I-MAVS signalling by fusogenic SARS-2-S.

SARS-2-S syncytium formation triggers the UPR-mediated accumulation of dsRNA recognized by RIG-I

We considered the possibility that RIG-I could be triggered by the accumulation of endogenous immunostimulatory RNAs. To test this hypothesis, we evaluated the levels of dsRNA in SARS-2-S syncytia using a specific, anti-dsRNA, monoclonal antibody J2. Notably, we observed increased dsRNA immunofluorescence signals in SARS-2-S syncytia at 3 hpc (Fig. 4a). In addition, some J2 foci colocalized with the mitochondria, indicating that the dsRNA detected in SARS-2-S syncytia by RIG-I may have originated from the mitochondria (Fig. 4a, b). Notably, over 70% of the dsRNA

colocalized with MAVS speckles in SARS-2-S syncytia (Fig. 4a, b). Therefore, we concluded that dsRNA triggers MAVS aggregation in SARS-2-S syncytia.

We next sought to characterize the source(s) of the RNA responsible for the activation of RIG-I-MAVS signalling in SARS-2-S syncytia. The UPR and consequent activation of IRE1α generate a pool of endogenous RNAs that trigger antiviral responses via RIG-I-MAVS[28]. We thus hypothesized that the mixing of the cytosolic contents of different cells might trigger the UPR to provoke RIG-I signalling by producing endogenous RNAs. Notably, RNA-seq analysis of cocultured cells revealed the enrichment of genes involved in ER stress at 2 hpc, indicating activation of the UPR at a very early stage during cell fusion (Fig. 4c). We then generated an XBP-1-enhanced green fluorescent protein (EGFP) reporter for ER stress as previously described[29]. Consistently, notable splicing of XBP-1 was observed in SARS-2-S syncytia as early as 2 hpc, and XBP-1 splicing gradually increased over time (Fig. 4d and Extended Data Fig. 6a, b). To examine whether the UPR regulates dsRNA accumulation, we treated cocultured cells with the chemical chaperone 4-phenylbutyric acid (4-PBA) to inhibit the UPR and found that UPR inhibition dramatically reduced the number and size of dsRNA puncta detected by immunostaining (Fig. 4d, e). In addition, MAVS aggregation and the expression of senescence-associated genes provoked by cell fusion were significantly blunted upon UPR inhibition (Fig. 4f, g). Consistently, we found that inhibiting dsRNA generation by *IRE1α* knockdown reduced MAVS aggregation in cocultured cells (Fig. 4h and Extended Data Fig. 6c). Together, these observations suggest that the activation of RIG-I-MAVS signalling in SARS-2-S syncytia is triggered

by its interaction with self-derived dsRNA generated by UPR activation.

MAVS-TNF-α signalling regulates the survival to senescence fate of SARS-2-S syncytia

We next attempted to identify factors that determine the senescence cell fate of SARS-2-S syncytia. To this end, we systematically analysed the gene expression of cocultured cells by RNA-seq at 4 and 48 hpc. Principal component analysis (PCA) of the data revealed that samples obtained after coculture for these durations did not overlap and were well separated from their respectively control (Fig. 5a). Gene Ontology (GO) enrichment analysis indicated that the coverage of senescence- and SASP-related GO terms increased with increasing coculture time (Fig. 5b). This finding supported the notion that fusogenic SARS-2-S gradually triggers a senescence stress response. Importantly, KEGG pathway analysis revealed enrichment in the TNF-α and NF-κB signalling pathways throughout the fusion process (Fig. 5c and Extended Data Fig. 7a, b). Notably, *MAVS* or *RIG-I* silencing significantly reduced the activation of NF-κB, IRF3, and TNF (Fig. 5d). Furthermore, the expression of *TNF* and *IL6* was also largely abolished in the MAVS KO, siRIG-I, or siMAVS cocultured 293T cells (Fig. 5e, f). In A549 cells with intact cGAS-STING signalling, syncytial survival and the senescent syncytial subpopulation were also significantly reduced by MAVS or RIG-I knockdown but not by STING knockdown (Fig. 5g, h). These results indicated the essential role of RIG-I-MAVS in regulating the fate of SARS-2-S syncytium.

To determine whether MAVS-mediated NF-κB signalling induction is required for the survival and senescence of SARS-2-S syncytia, we supplemented WT and MAVS

KO cocultured 293T cells with increasing concentrations of recombinant human TNF-α and IL-6. While pre-treatment with TNF-α and IL-6 before coculture did not affect SARS-2-S fusogenic potential (Fig. 5i), recombinant IL-6 at concentrations over 50 ng/mL improved the viability of MAVS KO cocultured cells, and recombinant TNF-α at concentrations above 0.05 ng/mL improved the viability of MAVS KO cocultured cells (Fig. 5j, k and Extended Data Fig. 8a, b). Notably, the percentage of SA-β-gal-positive syncytia was also significantly increased by TNF-α, especially in MAVS KO cells (Fig. 5l). TNF-α exerts its activity by stimulating its receptors, TNFR1 and TNFR2, which trigger distinct and common signalling pathways that control cell apoptosis and survival[30-32]. We observed that TNFR2 was selectively upregulated in cocultured 293T cells at both early and late stage of the fusion process (Extended Data Fig. 8c). Knockdown of *TNFR1* and *TNFR2* significantly reduced the viability of cocultured cells (Fig. 5m and Extended Data Fig. 8d). Remarkably, *TNFR1* knockdown blocked the increase of cocultured cells viability induced by TNF-α, but it was not as effective as *TNFR2* knockdown (Fig. 5n). Furthermore, neither *TNFR1* nor *TNFR2* deficiency affected SARS-2-S fusogenicity (Extended Data Fig. 8e). Taken together, these observations suggest that the MAVS-TNF-α-TNFR2 axis regulates the anti-death to senescence fate of SARS-2-S syncytia.

Massive accumulation of senescent SARS-2-S syncytia exerts a tumour-promoting effect

Senescent cells do not die and secrete a variety of proinflammatory factors and extracellular matrix-degrading enzymes. Hence, we wanted to assess the pathological

effect of the massive accumulation of senescent SARS-2-S syncytial cells by directly delivering SARS-2-S into ACE2-high human tumours. To this end, we chose human hepatocellular carcinoma (HCC) sample 1 with high ACE2 expression and established a PDX mouse model (Fig. 6a and Extended Data Fig. 9a). We used lentivirus-pseudotyped virus bearing SARS-2-S (SARS-2-Spp) or VSV-Gpp as control (Extended Data Fig. 9b). Mice bearing established HCC tumours with tumour volume of 160-190 mm^3 were treated with SARS-2-Spp or VSV-Gpp (Fig. 6a). In this model, SARS-2-Spp-injected tumours were larger and progressed more rapidly than VSV-Gpp-injected tumours (Fig. 6b-d), but no difference in mice weight was observed (Fig. 6e). Immunohistochemical detection of cell membrane NA^+/K^+-ATPase and nuclei DAPI staining revealed the presence of multinucleated cells in tumour section from SARS-2-Spp-treated mice, with relatively fewer multinucleated cells in tumour sections from VSV-Gpp-treated mice (Fig. 6f). Elevated tumour p21 staining and serum TNF-α and IL-6 levels supported the occurrence of SARS-2-S-elicited senescence (Fig. 6g, h). Strikingly, we detected one thymus metastatic foci in one SARS-2-S-treated mouse (Fig. 6i). Furthermore, the serum IL-6 and TNF-α levels in SARS-2-Spp mice with metastatic foci were higher than those in SARS-2-Spp mice without metastatic foci (Fig. 6h). Taken together, these findings suggested that the massive accumulation of senescent SARS-2-S syncytia exerted a tumour-promoting effect.

Discussion

As the main surface-exposed antigen and mediator of cell entry, the SARS-2-S protein also mediates cell-cell fusion via FFWI and FFWO manner. However, the pathological consequences and the regulation of those fused cells induced by fusogenic SARS-2-S remain poorly defined. Here, we directly linked SARS-2-S-triggered syncytium with the ensuing induction of cellular senescence, regardless of the cell type or syncytium nucleus number. SARS-2-S delivered by plasmid transfection in the form of mRNA or EVs triggered cell-cell fusion and a senescence-like phenotype. Notably, EVs containing SARS-2-S induced the formation of senescent syncytia in FFWO manner. In particular, SARS-2-S mRNA injection provoked the expression of genes involved in pathways related to senescence and the SASP *in vivo*. Further in-depth analysis indicated that SARS-S-2 senescence is regulated by the MAVS-TNF-α-TNFR2 axis and triggered by endogenous dsRNA that is generated by UPR activation in SARS-S-2 syncytia. Massive accumulation of senescent SARS-2-S syncytia exerted a tumour-promoting effect. Our findings thus may provide insight into the pathological consequences of fusogenic SARS-2-S in inducing senescence and reveal the critical role of the endogenous RNA-sensing pathway in determining the senescence fate of SARS-2-S syncytium.

Here, we show that the RIG-I-MAVS axis governs the fate of SARS-2-S syncytia. Although we cannot formally rule out the involvement of chromatin DNA and its sensors, cGAS and STING, in activating the senescence response induced by cell fusion, RIG-I-MAVS must play an essential role, because knockdown of MAVS or RIG-I, but

not STING, led to reduced syncytial survival and senescence. Similar to viral dsRNA, endogenous dsRNA activates the cellular dsRNA sensor RIG-I. Endogenous dsRNA originates from various sources, and cells utilize multiple mechanisms to suppress its biogenesis and accumulation. Here, we show that the majority of dsRNA molecules in SARS-2-S syncytia are of mitochondrial origin. We also detected some cytoplasmic dsRNA molecules, which might either have been introduced via mitochondrial leakage or be genome-derived. Regardless of the dsRNA source, our data link the activation of the UPR during cell fusion and dsRNA accumulation, functional RIG-I-MAVS signalling, and the survival and senescence of SARS-2-S syncytia. Interestingly, we observed robust MAVS aggregation during the fusion process, although it was accompanied by much weaker dsRNA signals. The underlying mechanism warrants further investigation. Overall, linking endogenous RNA sensing to the fate of SARS-2-S syncytia reveals an unexpected and unique aspect of RIG-like receptor-MAVS function. The formation of multinucleated giant cells following infection has been well documented for a long time. It would also be interesting to determine whether the described mechanism also operates in other host-pathogen contexts and represents a global mechanism.

We provide evidence of the contribution of RIG-I-MAVS to the regulation of SARS-2-S syncytium fate through TNF-α. Using multiplex protein analysis, we identified a burst of SASP-related cytokines, including TNF-α, IL-6, IFN-γ, and others, in the hACE2 mouse model injected with SARS-2-S mRNA and in the PDX mouse model injected with SARS-2-Spp. Although the exact contribution of each cytokine to

SARS-2-S syncytium survival and senescence is not clear, we provide evidence that the central regulation of SARS-2-S syncytium survival and senescence may be dependent on TNF-α. Indeed, *TNFR2* siRNA effectively reduced the increased survival of cocultured cells induced by TNF-α, highlighting the indispensable role of TNF-α in governing the fate of SARS-2-S syncytia mainly by TNFR2.

ACE2 is abundantly expressed on not only human lung and small intestine epithelial cells but also vascular endothelial cells, arterial smooth muscle cells, cardiomyocytes, cardiofibroblasts, and coronary endothelial cells[33, 34]. In addition, elevated expression of ACE2 has been observed across multiple tumour types[35-37]. Vaccination with the SARS-CoV-2 mRNA vaccine BNT162b2 and cell transfection with a SARS-2-S-expressing plasmid induced the production of exosomes harbouring SARS-2-S, which strongly suggests that cellular senescence induction by SARS-2-S might not be restricted to its expression site[15]. For example, even if a vaccine stays strictly in the muscle at the injection site, EVs that are produced in vaccinated patients may be able to trigger fusion in endothelial cells, neurons, or cardiomyocytes, resulting in thrombosis, neurological manifestations, or myocarditis[38]. In an exaggerated situation in which SARS-2-S expression was too high, the massive accumulation of senescent SARS-2-S syncytia exerted a tumour-promoting effect. Based on clinical findings, vaccines that use recombinant SARS-2-S fragments or other derivatives of SARS-2-S that are not fusogenic cause fewer complications than vaccines that express fully or partially fusogenic SARS-2-S[38]. To date, no evidence of syncytia has been identified in patients with long COVID-19 syndrome or in vaccinated people, and it

remains to be demonstrated whether the senescence phenotype and its pathological consequences observed in assay systems are of relevance for clinical long COVID-19 syndrome and the biology of actual vaccine effects. However, the primary fusogenic activity of SARS-2-S as an antigen should not be overlooked. The SARS-2-S protein is highly antigenic and has been subject to evolutionary pressure throughout the pandemic, leading to the rise of several variants with different fusogenicity. Novel SARS-CoV-2 variants with mutations associated with gains in syncytium formation should also be of great concern.

In summary, the presented data indicate that SARS-2-S-mediated fusion induces the UPR, which leads to the accumulation of dsRNA molecules that activate the cytosolic RNA-sensing RIG-I-MAVS pathway. The activation of functional MAVS aggregation, in turn, triggers the activation of NF-κB and thereby promotes the survival and senescence of SARS-2-S syncytia, mainly through TNF-α. We thus hypothesize that the induction of syncytium death by targeting TNF-α may be effective against long COVID-19 syndrome or adverse vaccination effects.

References

1. Lai, C.C., Shih, T.P., Ko, W.C., Tang, H.J. & Hsueh, P.R. Severe acute respiratory syndrome coronavirus 2 (SARS-CoV-2) and coronavirus disease-2019 (COVID-19): The epidemic and the challenges. *Int J Antimicrob Agents* **55**, 105924 (2020).
2. Bussani, R. *et al.* Persistence of viral RNA, pneumocyte syncytia and thrombosis are hallmarks of advanced COVID-19 pathology. *EBioMedicine* **61**, 103104 (2020).
3. Bourgonje, A.R. *et al.* Angiotensin-converting enzyme 2 (ACE2), SARS-CoV-2 and the pathophysiology of coronavirus disease 2019 (COVID-19). *J Pathol* **251**, 228-248 (2020).
4. Rajah, M.M., Bernier, A., Buchrieser, J. & Schwartz, O. The Mechanism and Consequences of SARS-CoV-2 Spike-Mediated Fusion and Syncytia Formation. *J Mol Biol* **434**, 167280 (2022).
5. Buchrieser, J. *et al.* Syncytia formation by SARS-CoV-2-infected cells. *EMBO J* **39**, e106267

(2020).
6. Zeng, C. *et al.* SARS-CoV-2 spreads through cell-to-cell transmission. *Proc Natl Acad Sci U S A* **119** (2022).
7. Zhou, Z. *et al.* Sensing of cytoplasmic chromatin by cGAS activates innate immune response in SARS-CoV-2 infection. *Signal Transduct Target Ther* **6**, 382 (2021).
8. Liu, X. *et al.* SARS-CoV-2 spike protein-induced cell fusion activates the cGAS-STING pathway and the interferon response. *Sci Signal* **15**, eabg8744 (2022).
9. Jackson, C.B., Farzan, M., Chen, B. & Choe, H. Mechanisms of SARS-CoV-2 entry into cells. *Nat Rev Mol Cell Biol* **23**, 3-20 (2022).
10. Theuerkauf, S.A. *et al.* Quantitative assays reveal cell fusion at minimal levels of SARS-CoV-2 spike protein and fusion from without. *iScience* **24**, 102170 (2021).
11. Lopez Bernal, J. *et al.* Effectiveness of the Pfizer-BioNTech and Oxford-AstraZeneca vaccines on covid-19 related symptoms, hospital admissions, and mortality in older adults in England: test negative case-control study. *BMJ* **373**, n1088 (2021).
12. Al Khames Aga, Q.A. *et al.* Safety of COVID-19 vaccines. *J Med Virol* **93**, 6588-6594 (2021).
13. Rosenblum, H.G. *et al.* Use of COVID-19 Vaccines After Reports of Adverse Events Among Adult Recipients of Janssen (Johnson & Johnson) and mRNA COVID-19 Vaccines (Pfizer-BioNTech and Moderna): Update from the Advisory Committee on Immunization Practices - United States, July 2021. *MMWR Morb Mortal Wkly Rep* **70**, 1094-1099 (2021).
14. Ogata, A.F. *et al.* Circulating Severe Acute Respiratory Syndrome Coronavirus 2 (SARS-CoV-2) Vaccine Antigen Detected in the Plasma of mRNA-1273 Vaccine Recipients. *Clin Infect Dis* **74**, 715-718 (2022).
15. Bansal, S. *et al.* Cutting Edge: Circulating Exosomes with COVID Spike Protein Are Induced by BNT162b2 (Pfizer-BioNTech) Vaccination prior to Development of Antibodies: A Novel Mechanism for Immune Activation by mRNA Vaccines. *J Immunol* **207**, 2405-2410 (2021).
16. Swank, Z. *et al.* Persistent circulating SARS-CoV-2 spike is associated with post-acute COVID-19 sequelae. *Clin Infect Dis* (2022).
17. Lee, S. *et al.* Virus-induced senescence is a driver and therapeutic target in COVID-19. *Nature* **599**, 283-289 (2021).
18. Kumari, R. & Jat, P. Mechanisms of Cellular Senescence: Cell Cycle Arrest and Senescence Associated Secretory Phenotype. *Front Cell Dev Biol* **9**, 645593 (2021).
19. Tsuji, S. *et al.* SARS-CoV-2 infection triggers paracrine senescence and leads to a sustained senescence-associated inflammatory response. *Nature Aging* **2**, 115-124 (2022).
20. Seoane, R., Vidal, S., Bouzaher, Y.H., El Motiam, A. & Rivas, C. The Interaction of Viruses with the Cellular Senescence Response. *Biology (Basel)* **9** (2020).
21. Hoffmann, M., Kleine-Weber, H. & Pohlmann, S. A Multibasic Cleavage Site in the Spike Protein of SARS-CoV-2 Is Essential for Infection of Human Lung Cells. *Mol Cell* **78**, 779-784 e775 (2020).
22. Hornich, B.F. *et al.* SARS-CoV-2 and SARS-CoV Spike-Mediated Cell-Cell Fusion Differ in Their Requirements for Receptor Expression and Proteolytic Activation. *J Virol* **95** (2021).
23. Suzuki, R. *et al.* Attenuated fusogenicity and pathogenicity of SARS-CoV-2 Omicron variant. *Nature* **603**, 700-705 (2022).
24. Zhang, Y. *et al.* The DNA sensor, cyclic GMP-AMP synthase, is essential for induction of IFN-beta during Chlamydia trachomatis infection. *J Immunol* **193**, 2394-2404 (2014).
25. Rehwinkel, J. & Gack, M.U. RIG-I-like receptors: their regulation and roles in RNA sensing. *Nat*

Rev Immunol **20**, 537-551 (2020).
26. Jia, Y. *et al.* Negative regulation of MAVS-mediated innate immune response by PSMA7. *J Immunol* **183**, 4241-4248 (2009).
27. Li, D. *et al.* Novel Insights and Current Evidence for Mechanisms of Atherosclerosis: Mitochondrial Dynamics as a Potential Therapeutic Target. *Front Cell Dev Biol* **9**, 673839 (2021).
28. Reverendo, M., Mendes, A., Arguello, R.J., Gatti, E. & Pierre, P. At the crossway of ER-stress and proinflammatory responses. *FEBS J* **286**, 297-310 (2019).
29. Ryoo, H.D., Domingos, P.M., Kang, M.J. & Steller, H. Unfolded protein response in a Drosophila model for retinal degeneration. *EMBO J* **26**, 242-252 (2007).
30. Wajant, H. & Siegmund, D. TNFR1 and TNFR2 in the Control of the Life and Death Balance of Macrophages. *Front Cell Dev Biol* **7**, 91 (2019).
31. Naude, P.J., den Boer, J.A., Luiten, P.G. & Eisel, U.L. Tumor necrosis factor receptor cross-talk. *FEBS J* **278**, 888-898 (2011).
32. Holbrook, J., Lara-Reyna, S., Jarosz-Griffiths, H. & McDermott, M. Tumour necrosis factor signalling in health and disease. *F1000Res* **8** (2019).
33. Hikmet, F. *et al.* The protein expression profile of ACE2 in human tissues. *Mol Syst Biol* **16**, e9610 (2020).
34. Li, M.Y., Li, L., Zhang, Y. & Wang, X.S. Expression of the SARS-CoV-2 cell receptor gene ACE2 in a wide variety of human tissues. *Infect Dis Poverty* **9**, 45 (2020).
35. Liu, C. *et al.* High expression of ACE2 and TMPRSS2 and clinical characteristics of COVID-19 in colorectal cancer patients. *NPJ Precis Oncol* **5**, 1 (2021).
36. Dai, Y.J. *et al.* A profiling analysis on the receptor ACE2 expression reveals the potential risk of different type of cancers vulnerable to SARS-CoV-2 infection. *Ann Transl Med* **8**, 481 (2020).
37. Nair, M.G., Prabhu, J.S. & Ts, S. High expression of ACE2 in HER2 subtype of breast cancer is a marker of poor prognosis. *Cancer Treat Res Commun* **27**, 100321 (2021).
38. Lazebnik, Y. Cell fusion as a link between the SARS-CoV-2 spike protein, COVID-19 complications, and vaccine side effects. *Oncotarget* **12**, 2476-2488 (2021).
39. Ickenstein, L.M. & Garidel, P. Lipid-based nanoparticle formulations for small molecules and RNA drugs. *Expert Opin Drug Deliv* **16**, 1205-1226 (2019).
40. Xiong, Y. *et al.* Effects of microRNA-29 on apoptosis, tumorigenicity, and prognosis of hepatocellular carcinoma. *Hepatology* **51**, 836-845 (2010).

Methods

Reagents

Dulbecco's modified Eagle's medium (DMEM, high-glucose, D5796) and protease inhibitor cocktail I (20-201) were purchased from Millipore (Massachusetts, USA). Foetal bovine serum (FBS, A3160901) was purchased from Gibco (New York, USA). Lipofectamine™ 2000 (11668-027), MitoTracker™ Deep Red FM and CellEvent™

Senescence Green detection kit (C10850) were purchased from Invitrogen (Massachusetts, USA). BCA protein concentration determination kit (P0012), DAPI (C1002) and β-galactosidase reporter gene assay kit (RG0036) were purchased from Beyotime (Shanghai, China). NucleoZOL (740404) was purchased from MACHEREY-NAGEL (MN, Düren, Deutschland). PerfectStart^{TM} Green qPCR SuperMix (AQ601) and TransScript® One-Step gDNA Removal and cDNA Synthesis SuperMix (AT311) were purchased from TransGen Biotech (Beijing, China). 4-PBA (HY-A0281), Fisetin (S2298), Dasatinib (S1021) and Venetoclax (S8048) were purchased from Selleck Chemicals (Houston, TX). Recombinant human IL-6 (AF-200-06) and human TNF-α (300-01A) were purchased from PeproTech (New Jersey, USA).

Antibodies

Anti-CD81 (ab109201, 1:1,000 dilution), anti-CD63 (ab134045, 1:1,000 dilution), anti-TSG101 (ab125011, 1:1,000 dilution), anti-CD9 (ab263019, 1:1,000 dilution), anti-ACE2 (ab108252, 1:1,000 dilution) and anti-IRF3 (ab76409, 1:1000 dilution) were purchased from Abcam (Cambridge, UK). Anti-α-tubulin (T9026, 1:5,000 dilution) and anti-Flag (A8592, 1:10,000 dilution) were purchased from Sigma-Aldrich (Missouri, USA). Anti-TNF-α (60291-1-Ig, 1:5,000 dilution), anti-MAVS (14341-1-AP, 1:100 dilution for immunofluorescence, 1:4,000 dilution for immunoblotting), anti-TRAF3 (18099-1-AP, 1:1,000 dilution), anti-p21 (10355-1-AP, 1:100 dilution), anti-p16 (10883-1-AP, 1:100 dilution), anti-TBK1 (28397-1-AP, 1:2,000 dilution), anti-STING (19851-1-AP, 1:3,000 dilution) and anti-GAPDH (60004-4-I-Ig, 1:5,000 dilution) were purchased from Proteintech (Wuhan, China). Anti-SARS-CoV/SARS-2-S

(GTX632604, 1:2,000 dilution) was purchased from GeneTex (CA, USA). Anti-TRAF6 (8028S, 1:1,000 dilution), anti-phospho-p65 (3033T, 1:1,000 dilution), anti-RIG-I (3743T, 1:1,000 dilution), anti-phospho-IRF3 (4947S, 1:1,000 dilution) and anti-phospho-TBK1 (5483T, 1:2,000 dilution) were purchased from Cell Signaling Technology (Massachusetts, USA). Anti-phospho-p65 (A19653, 1:1,000 dilution) was purchased from ABclonal (Wuhan, CHINA). Anti-rabbit HRP-IgG (ZB-2301, 1:5,000 dilution) and anti-mouse HRP-IgG (ZB-2305, 1:5,000 dilution) were purchased from ZSGB-BIO (Beijing, China).

Plasmids, cell culture and small interfering RNAs (siRNAs)

Mammalian expression vectors encoding SARS-2-S (Wuhan-Hu-1, GenBank: NC_045512.2), SARS-2-SNF (spike R682A, R683A, R685A, K814A and R815A) and SARS-2-SO (Omicron) were codon-optimized and cloned into the pcDNA3.1 expression vector. To produce lentivirus plasmids, SARS-2-S and ACE2 were cloned into the pCDH-CMV-MCS-EF1-Puro vector. pEGFP-N1-XBP-1, NF-κB-Luc, IFN-β-Luc, and IRF-3-Luc reporter gene constructs were kept in our laboratory. All plasmids were verified by DNA sequencing.

The A549 (CRL-185), HEK293T (CRL-3216), HeLa (CRL-3216) and HIEC-6 (CRL-3266) cell lines were obtained from the American Type Culture Collection (ATCC, Rockville, MD, USA). MAVS-KO 293T cells were kindly provided by T. Li (National Center of Biomedical Analysis, Beijing, China). All cell lines were mycoplasma free and incubated in DMEM supplemented with 10% FBS, 100 U/mL penicillin, and 0.1 mg/mL streptomycin at 37°C under a humidified atmosphere with 5% CO_2.

Lipofectamine™ 2000 was used for transfection following the manufacturer's protocol. For lentivirus production, pMD2.G, psPAX2 and pCDH-SARS-2-S/pCDH-ACE2 were transfected into 293T cells together and lentiviral particles were harvested from cell supernatants filtered through a 0.45 μm filter 48 h later. For stable overexpression of ACE2 and SARS-2-S, 293T, A549, HIEC-6 and HeLa cells were infected with harvested lentiviral particles and selected in the presence of puromycin (2-4 μg/mL). Stably transfected clones were selected under puromycin pressure after two weeks. To knock down specific genes, siRNAs targeting human genes were purchased from GenePharma, and their target sequences are listed in Table S1.

β-galactosidase reporter gene assay

To quantify the cell-cell fusion level, an α-complementation of lacZ system based on β-galactosidase was used[10]. Producer cells were constructed with SARS-2-S and lacZ (△11-41aa) and target cells were constructed with ACE2 and lacZ (1-56aa). Upon cell-cell fusion, complementation of lacZ (△11-41aa) with lacZ (1-56aa) inside the syncytium results in the formation of active β-galactosidase that is then quantified by a β-galactosidase Reporter Gene Assay Kit as manufacturer's instruction. Briefly, 50 μL lysates collected from syncytium at the indicated times were added equal amounts of specific substrate 2-Nitrophenyl β-D-galactopyranoside (ONPG). After 3 h incubation, the reactions were quenched by 150 μL stop solution and the absorbance was measured at 420 nm using a on a multimode microplate reader (Tecan).

SARS-2-S-mRNA-LNP synthesis

T7 RNA polymerase-mediated transcription from a linearized DNA template from a

plasmid that encodes codon-optimized SARS-2-S was used to produce mRNA *in vitro*. Lipid-nanoparticle (LNP) formulations were prepared using a method previously described for siRNA[39] with modifications. Briefly, lipids were dissolved in ethanol containing an ionizable lipid, 1,2-distearoyl-sn-glycero3-phosphocholine (DSPC), cholesterol and PEG-lipid (at molar ratios of 50:10:38.5:1.5). The lipid mixture was combined with 20 mM citrate buffer (pH 4.0) containing mRNA at a ratio of 1:2 through a T-mixer. The formulations were then diafiltrated against a 10 × volume of PBS (pH 7.4) through a tangential-flow filtration (TFF) membrane with a 100 kD molecular weight cut-off (Sartorius Stedim Biotech), concentrated to the desired concentrations, and passed through a 0.22-mm filter. All formulations were tested for particle size, distribution, RNA concentration and encapsulation.

EV purification

For EV production, supernatants of HeLa and SARS-2-S stable transfected HeLa cells cultured in EV-depleted medium were collected after 72 h and centrifuged at 300 × g for 10 min to remove the cells. The cell supernatant was diluted 1:2 with cold PBS before low-speed centrifugation at 3000 × g for 10 min, and the resulting supernatant was transferred to new tubes for ultracentrifugation at 100,000 ×g using a type 100 TI rotor in an XPN-100 instrument (CP100NX; Hitachi, Brea, USA) for 90 min. The resulting EV pellet was resuspended in 250 mL of cold PBS and denoted EVs.

Flow cytometry

To assess the cellular uptake of S-EVs, the cells were exposed to DiO-labelled EVs at the indicated doses and then incubated at 37°C for the indicated durations. After

extensive washing, flow cytometry was performed with an Attune® NxT instrument (Thermo Fisher Scientific, Massachusetts, USA), and 30,000 cell acquisitions under a medium flow rate were used for data capture. Data analysis was performed using FlowJo software (V10.0.7r2). A control sample consisting of DiO dye used as the background was prepared following the same procedure indicated above.

For SARS-2-S protein expression, cells were treated with S-EVs. Forty hours later, the cells were detached and incubated with SARS-2-S mAb (GTX632604, clone 1A9, 1:1,000 dilution) for 30 min on ice, followed by incubation with PE goat anti-mouse IgG (Biolegend, 405307, 1:100 dilution) for 15 min at room temperature. The cells were then analysed by flow cytometry.

Multiplex bead-based protein detection (MAGPIX)

Multiplex bead-based protein analyses were conducted according to the manufacturer's instructions with a custom Procartaplex 36-plex panel (Thermo Fisher Scientific, cat. no. EPX360-26092-901). Briefly, samples were diluted, and 50 µl of each prepared sample was incubated with antibody-conjugated magnetic beads and incubated for 1 h overnight at 4°C. After washing, detection antibodies were added and incubated at room temperature for 30 min. Following further washing steps, PE-streptavidin was added and incubated for 30 min. The assay data were measured with the Bio-Plex® MAGPIX™ multiplex reader (Bio-Rad) and analysed with a 5PL algorithm provided by Bio-Plex Manager™ software (version 6.1).

Semi-denaturing detergent agarose gel electrophoresis (SDD-AGE)

Crude mitochondria and cytosolic extracts were separated from A549 cells using

differential centrifugation with a cell mitochondria isolation kit (Beyotime, C3601) according to a published protocol[40]. A549 cells were resuspended and lysed by grinding, and were centrifuged at 800 × g for 10 min at 4°C. The supernatants were transferred to a new tube and centrifuged at 13,000 × g for 10 min at 4°C to separate the crude mitochondria and cytosolic extracts. The crude mitochondria were resuspended in sample buffer (0.5 × TAE, 10% glycerol, 2% SDS, and 0.0025% bromophenol blue) and loaded onto a 1.5% agarose gel. Then, the samples were electrophoresed at a constant voltage of 80 V at 4°C. The proteins were transferred to PVDF membranes for immunoblotting.

Luciferase reporter assays

A luciferase expression vector controlled by a promoter containing three repeats of the NF-κB response element was obtained from Beyotime (D2204). The pSV40-Renilla plasmid was purchased from Promega (E2231). To assess the activity of NF-κB, cells were plated in triplicate in a 24-well plate and then transiently transfected with pNF-κB-luc and the internal control plasmid pSV40-Renilla for 12 h. The cells were then cocultured for the indicated durations. The cells were harvested, and firefly luciferase activity and Renilla luciferase activity were detected using the dual-luciferase reporter assay system (Promega, E1910) with a multimode microplate reader (Tecan). The firefly luciferase luminescence data were normalized to the Renilla luciferase luminescence data.

VSV infection

Cells were plated in 12-well plates, and VSV was added to the medium at a

concentration of 80 haemagglutinating units per mL and a multiplicity of infection (MOI) of 5 at 60% cell confluence. After 1 h of incubation, the extracellular virus was removed by washing the cells twice with serum-containing medium. Cells were fixed at the indicated times after infection for immunofluorescence assays.

Cell–cell fusion assay

Cells were stably transfected with SARS-2-S or ACE2 and cultured to 60% confluence. Then, SARS-2-S-expressing cells and ACE2-expressing cells were either mixed at 1:1 ratios or allowed to continue culture. At the indicated times, the cocultured cells were harvested, and the individually cultured SARS-2-S-expressing cells and ACE2-expressing cells were mixed *in vitro* using the same ratio used for the non-fusion controls.

Syncytia viability assay

A CCK8 assay was used to assess syncytia cell viability. Briefly, cocultured cells were seeded into a 96-well plate at a cell density of 3000 per well and allowed to adhere for 72 h. Then, the medium was washed and replaced with fresh medium, followed by treatment with serially diluted inhibitors. At 24 h after treatment, 10 μL of CCK-8 solution was added to 100 μL of culture medium, and the absorbance of each well was measured at 450 nm using a multimode microplate reader (Tecan) with Tecan Spark Control (v.2.1) software. All experiments were performed in triplicate, and the cell viability was calculated as the ratio of the viability under each experimental condition to the viability of the control.

Animals

Male C57BL/6N WT mice (8 to 10 weeks old) were purchased from SPF Biotechnology (Beijing, China). All mice were conventionally group-housed on a 12-h light/dark cycle in an animal facility for 3 days before any procedures. For S-mRNA-LNP injections, we injected 3.0 x 10^{11} μg/mouse AAV-hACE2 constructs into the tail veins of 8-week-old C57BL/6 mice to drive mainly hepatic hACE2 expression. Four weeks later, the mice were administered 3.0 μg of S-mRNA-LNP or LNP via i.m. injection, followed by terminal sacrifice of the mice and the collection of sera and livers at the indicated times. For the PDX mouse model, female immune-deficient NOD/SCID mice (6 to 8 weeks old) (GemPharmatech, Nanjing, China) were chosen for PDX model development at Crown Bioscience (Zhongshan, China). Fresh liver tumour tissues were cut into small pieces (2-3 mm in diameter) and then subcutaneously transplanted into the right flanks of mice. Lentiviruses that encode the VSV-G protein or SARS-2-S protein were manufactured by VectorBuilder (Guangzhou, China). The pMD2.G, psPAX2 and pLV-eGFP-VSV-G or pLV-eGFP-SARS-2-S) vectors were transfected into HEK293T cells. At 48 h after transfection, lentiviruses were harvested, concentrated by centrifugation at 50,000 ×g in 20% (w/v) sucrose solution and titrated. Once tumours grew to have a volume of 160-190 mm^3, lentiviruses were injected intratumorally (i.t.) at the indicated days at 1.3 x 10^7 TU/mouse. Mouse serum and tumours were collected for further study after the mice had been terminally sacrificed. All animal studies were performed according to standard operating procedures in a specific pathogen-free facility under the approval of the Institutional Animal Care and Use Committee.

Quantitative real-time PCR (RT–qPCR)

Total mRNA was extracted from cells or tissues using NucleoZOL. cDNA was prepared from total mRNA by using TransScript® One-Step gDNA Removal and cDNA Synthesis SuperMix, and the relative amounts of individual mRNAs were calculated after normalizing to corresponding β-actin mRNA, as previously described. The primer sequences are included in Table S2.

Western blotting and immunoprecipitation

Cells were lysed in NP40 cell lysis buffer with fresh protease inhibitors. Supernatants were separated by SDS–PAGE after centrifugation and transferred to PVDF membrane for immunoblot analyses using the indicated antibodies.

Whole-cell lysates (WCLs) for coimmunoprecipitation were prepared by sonication in NP40 buffer (1% NP40, 150 mM NaCl and 40 mM Tris pH 7.5). Clarified lysates were then incubated with the indicated antibodies and then with Protein A/G PLUS-agarose. After four washes with PBS, the immunoprecipitates were collected by centrifugation and reserved for immunoblot analyses.

RNA-sequencing (RNA-seq) analysis

Total RNA was isolated from cells or liver tissues with TRIzol reagent, and the RIN was checked to inspect RNA integrity with an Agilent 2100 Bioanalyzer (Agilent Technologies, Santa Clara, CA, US). The qualified total RNA was further purified with an RNAClean XP kit (cat No. A63987, Beckman Coulter, Inc., Kraemer Boulevard, Brea, CA, USA) and RNase-Free DNase Set (cat# 79254, QIAGEN, GmBH, Germany). cDNA libraries were constructed following Illumina standard protocols and sequenced

with an Illumina NovaSeq 6000 by SHBIO (Shanghai, China). The sequencing reads were mapped to the human genome using TopHat (version 1.0.13). Avadis NGS (version 1.3) was used to calculate reads per kilobase per million mapped reads (RPKM) values. P-value and fold-change (FC) in the expression of genes between groups were jointly used to identify differentially expressed genes (DEGs). The criterion of statistical significance was $P < 0.05$ and $|Log2(FC)| > 1$. GO enrichment and KEGG pathway analysis were conducted by SHBIO to investigate the potential functions of the DEGs, and $P < 0.05$ was considered to indicate a statistically significant difference.

Immunofluorescence analysis

For immunofluorescence staining, cells or tissue sections were fixed with a 4% paraformaldehyde solution, washed twice with PBS and permeabilized with 0.3% Triton X-100 in PBS. The Triton X-100 solution was replaced with 5% (w/v) BSA and samples were incubated with primary antibodies for 1 h. After washing three times with PBST (0.05% Tween 20 in PBS), the samples were incubated with fluorophore-conjugated secondary antibodies diluted in PBS for 30 min. After washing three times with PBST, the nuclei were labelled with a DAPI solution. For dsRNA staining assays, J2 was used as the primary antibody, and Alexa Fluor™ 555-labelled donkey anti-mouse IgG (H+L) secondary antibody was used as the secondary antibody.

For SA-β-gal staining assays, SA-β-gal was detected with the CellEvent™ Senescence Green Probe under a fluorescence microscope. Fluorescent images were acquired under a Nikon A1 confocal microscope, Zeiss LSM710 confocal microscope or Tecan Spark Cyto. The images were processed and analysed using Volocity (v.6.1.1, PerkinElmer),

Nikon NIS-Elements AR (v4.00.12) or ImageJ (version 1.53c).

Statistical analysis

In the present study, GraphPad Prism 8.0 was used for statistical calculations and data plotting. Differences between two independent samples were evaluated by two-tailed Student's t tests or the Mann–Whitney test, as appropriate. Differences between multiple samples were analysed by one-way ANOVA or two-way ANOVA, followed by Bonferroni's post hoc analysis, as appropriate. All tests were two-tailed, unless otherwise indicated. We considered a P value<0.05 to indicate statistical significance. Significance values were set as follows: ns (not significant), $P > 0.05$; *, $P < 0.05$; **, $P < 0.01$; ***, $P < 0.001$.

Data availability

The numeric source data are provided in source data files, and all of the other data that support the findings of this study are available from the corresponding author upon reasonable request. The RNA-seq data have been deposited in the NCBI Sequence Read Archive (SRA) and are accessible through accession numbers PRJNA884818, PRJNA881496 and PRJNA880840.

Acknowledgements

We thank the Development Program of China (grant No. 2022YFC2600100) and National Natural Science Foundation of China (grant Nos. 32270823, 31872715 and 32070755) conducted by H. Zhong, the National Natural Science Foundation of China (grant Nos. 81773205 and 82070595) conducted by C. W. Wei, the National Natural Science Foundation of China (grant No. 32100558) conducted by L. M. Wan and the Postdoctoral Science Foundation of China (grant No. 2020M683743) conducted by X.

P. Yang. A graphical abstract was created and exported with BioRender.com under a paid subscription.

Author contributions

H.Z., C.W.W., L.M.W., Q.G. and L.H.H. designed the experiments. L.M.W., H.L.L., L.F.H., M.Y.L., J.F.L., J.L.L., Y.H.Z., C.W.W. and H.Z. collected and analysed the data. H.L.L., L.F.H., M.Y.L., Q.L.Y., J.F.L. and J.L. carried out the mouse assays. L.M.W., L.F.H., Y.L.Y., M.Y.L., R.Z.Z., X.P.Y., J.L. L and J.F.L. carried out the cell line experiments. L.J.S., X.F.H. and X.H.Z. provided key experimental materials. Q.G., J.J.X., L.H.H., C.W.W. and H.Z. prepared the manuscript.

Completing interests

The authors declare no competing interests.

Figures and Figure legends

Fig. 1

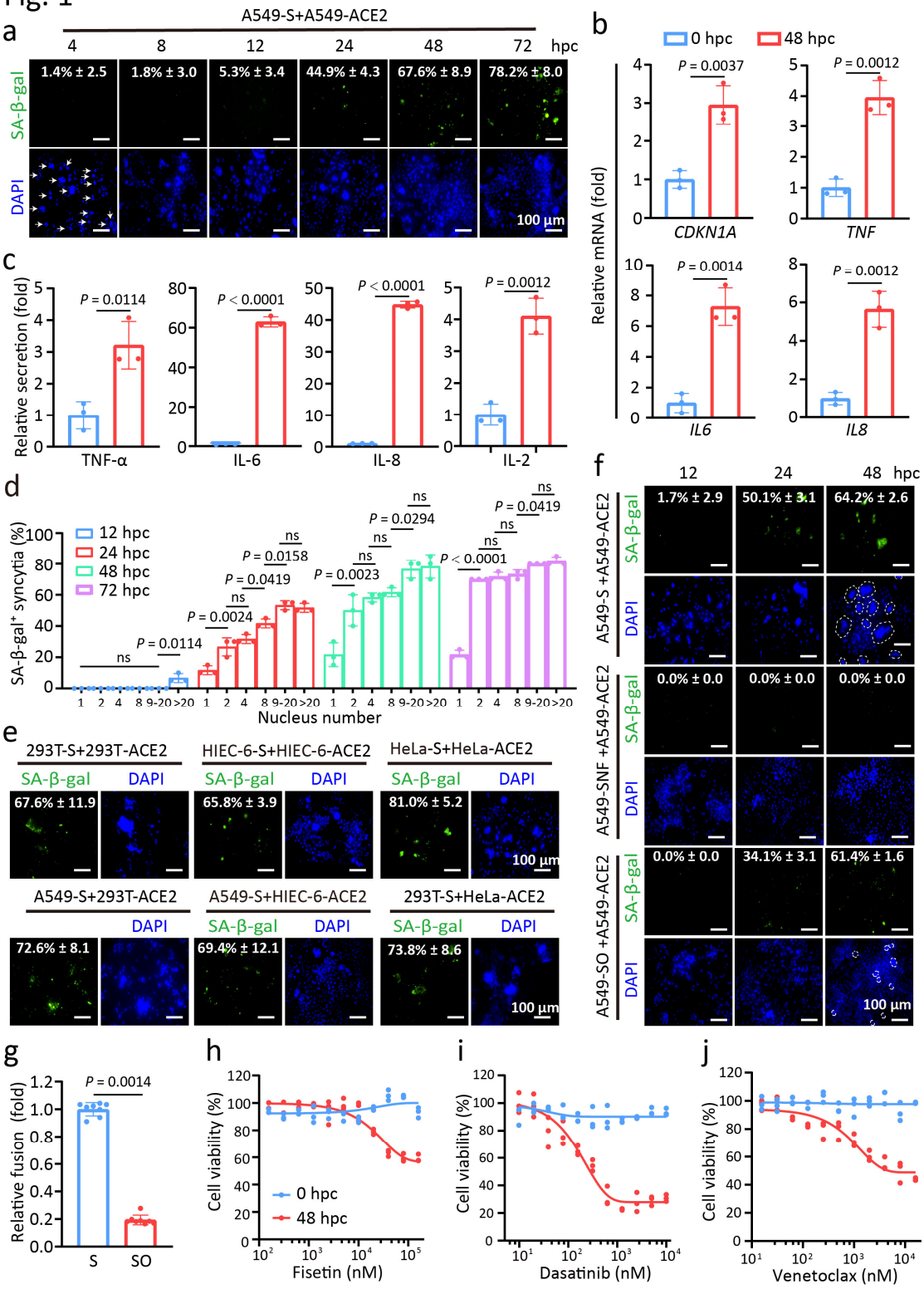

Fig. 1| SARS-2-S–expressing syncytia exhibit a senescence-like phenotype. a, SA-β-gal staining of A549-SARS-2-S (SARS-2-S hereafter referred to S) and A549-ACE2

cells cocultured for the indicated h (hpc). Green, SA-β-gal staining; blue, nuclear DAPI staining. Scale bars represented 100 μm. **b,** Normalized expression of *CDKN1A*, *TNF*, *IL6*, and *IL8* transcripts in cocultured A549 cells at 48 hpc relative to that at 0 hpc by RT–qPCR. **c**, TNF-α, IL-6, IL-8, and IL-2 protein levels in conditioned medium from cells in **b** by ELISA. **d,** Quantification of SA-β-gal positivity in cocultured A549 cells with different nuclei numbers during fusion for the indicated hpc. **e,** SA-β-gal staining of S–expressing cells cocultured with the same (upper) or different cell types (lower). Scale bars represented 100 μm. **f,** SA-β-gal staining of S, SNF (R682A, R683A, R685A, K814A, and R815A mutant), or SO (Omicron spike)-transfected A549 and A549-ACE2 cells cocultured for the indicated hpc. Scale bars represented 100 μm. **g,** Quantification of the relative fusion ability of SO. The numbers of SO syncytia at 24 hpc was normalized to the syncytia numbers of S by DAPI staining in **f**. **h-j,** Cell viability of cocultured A549 cells at 24 hpc treated with Fisetin **(h)**, Dasatinib **(i),** or Venetoclax **(j)** for 12 h by CCK8 assay. All images were representative of 3 biological replicates. All quantified data were presented as the mean ± SD of n = 3 independent experiments. Statistical significance was determined using two-tailed Student's *t test* (**b**, **c, g**) or one-way ANOVA and Bonferroni's post hoc analysis (**d**).

Fig. 2

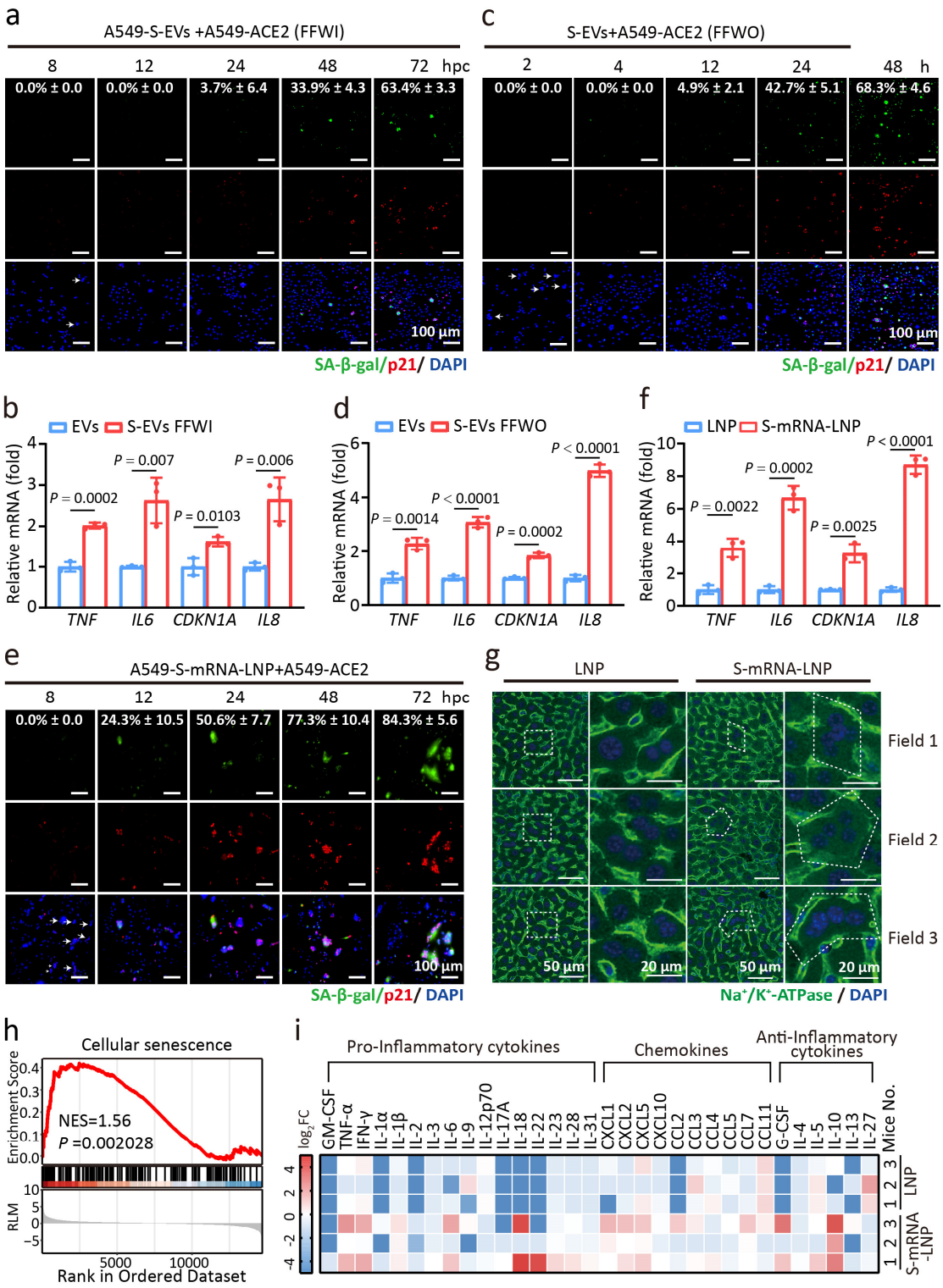

Fig. 2| SARS-2-S delivery by EVs or mRNA triggers syncytial senescence. a,c,e, SA-β-gal and p21 staining of A549-S-EVs and A549-ACE2 cocultured cells (a, fusion from within (FFWI)) or A549-ACE2 cells treated with S-EVs (c, fusion from without

(FFWO)) or A549-S-mRNA-LNP and A549-ACE2 cocultured cells (e) for the indicated times. Green, SA-β-gal staining; red, p21 staining; blue, DAPI staining. Scale bars represented 100 μm. **b,d,f,** Normalized expression of *TNF*, *IL6, CDKN1A, and IL8* in A549 cells at 24 hpc from **a** (**b**), **c** (**d**), and e (**f**) relative to that at 0 hpc by RT-qPCR. **g,** Immunohistochemical analysis of liver tissues from mice i.m. injected with a single dose of S-mRNA-LNP (0.12 mg/kg) or LNP at 24 h after injection. Green, Na^+/Ka^+-ATPase staining for cell membrane; blue, nuclear DAPI staining. Scale bars represented 50 μm or 20 μm as indicated. **h,** Gene set enrichment analysis (GSEA) of genes related to cellular senescence in the livers from mice in **g**. NES, normalized enrichment score; RLM, ranked list metric. **i,** Multiplex bead-based protein analysis in the serum from mice in **g**. All images were representative of 3 biological replicates. All quantified data were presented as the mean ± SD of n = 3 independent experiments. Statistical significance was determined using two-tailed Student's *t* test (**b**, **d, f**).

Fig.3

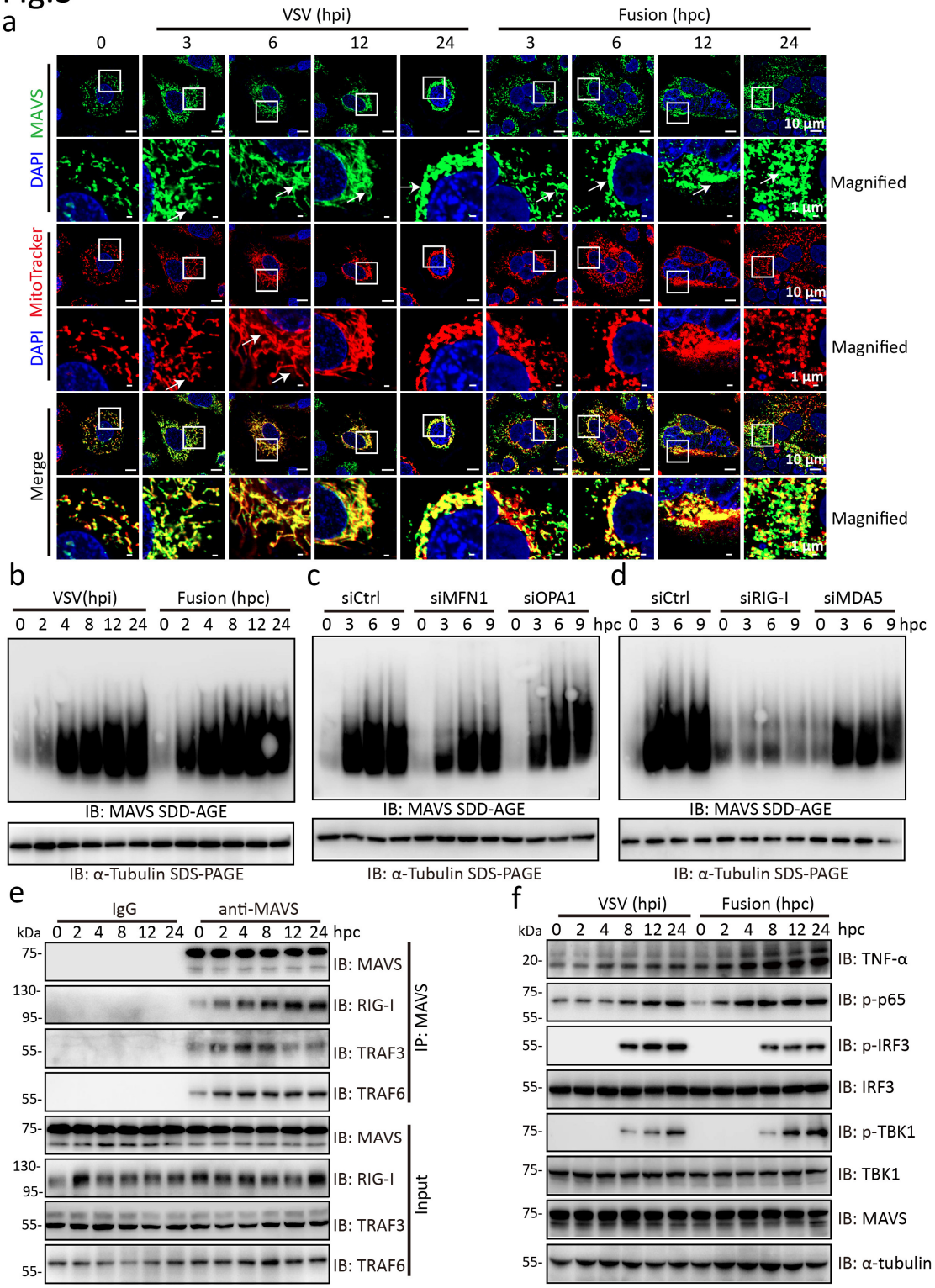

Fig. 3| SARS-2-S syncytia induce the RIG-I–dependent formation of functional MAVS aggregates. a, Confocal microscopic images of MAVS and mitochondria in A549 cells infected with VSV or A549 cells cocultured for the indicated times. Red,

MitoTracker staining for mitochondria; green, MAVS staining; blue, DAPI staining. A magnified view of the boxed region was also shown. Scale bars represented 10 μm (whole image) and 1 μm (magnified). **b,** MAVS aggregation in VSV-infected A549 cells or A549 cells cocultured for the indicated times by SDD-AGE with an anti-MAVS antibody. SDS-PAGE immunoblotting of α-tubulin was used as a loading control. **c, d,** MAVS aggregation in sicontrol (siCtrl), siMFN1, and siOPA1 (**c**) or siCtrl, siRIG-I, and siMDA5 (**d**) A549 cells cocultured for the indicated times. All these siRNA oligos were transfected to A549-S and A549-ACE2 cells 24 h before coculture start. α-tubulin used as the loading control. MAVS aggregates were analysed by SDD-AGE as in **b**. **e,** Immunoprecipitation analysis of MAVS interaction with RIG-I, TRAF3, and TRAF6 in A549 cells cocultured for the indicated times. **f,** Immunoblotting analysis of proteins of activated IFN-I signalling pathway in VSV-infected A549 cells or A549 cocultured cells for the indicated times.α-tubulin used as the loading control. All images were representative of three independent experiments.

Fig. 4

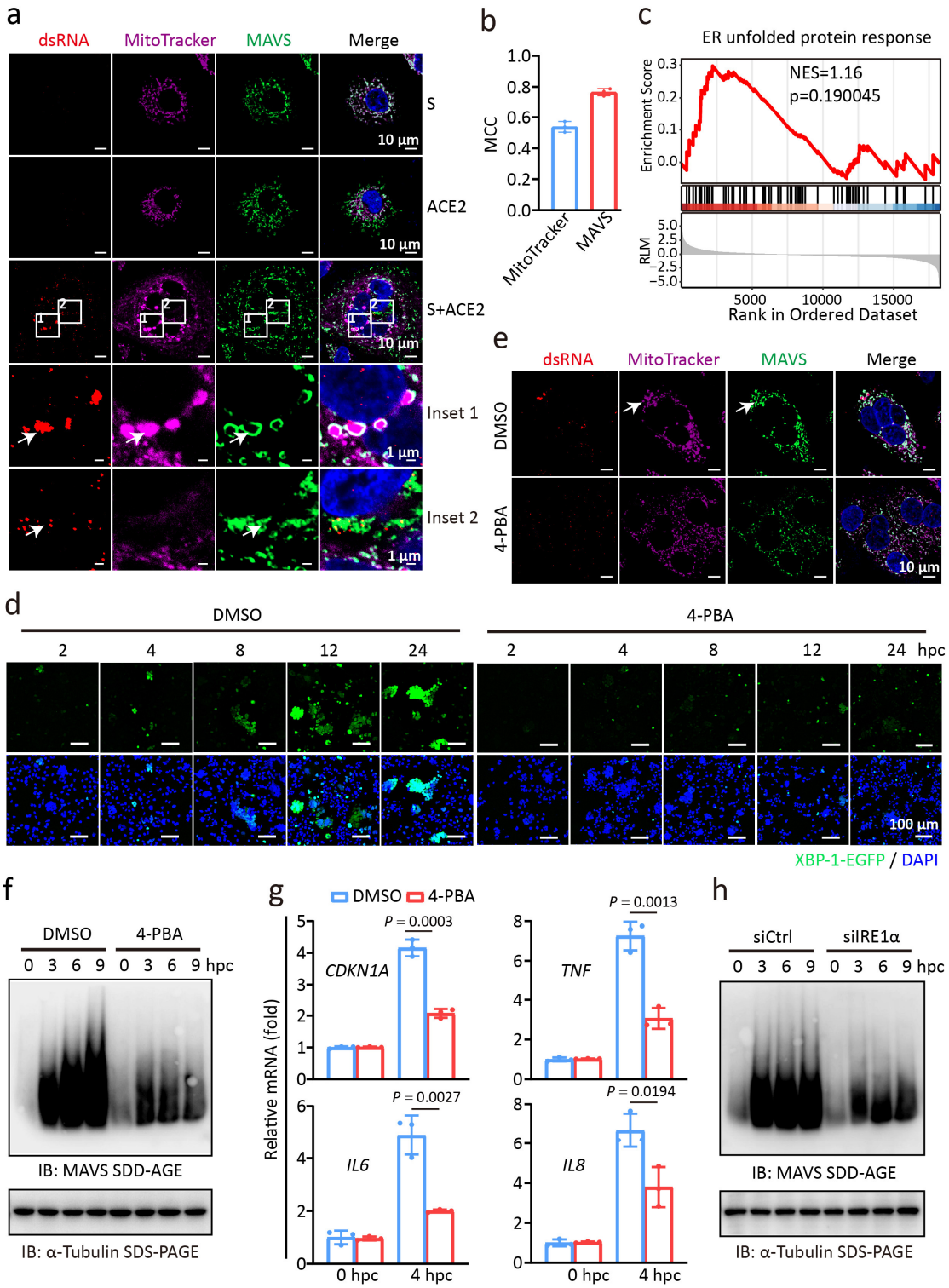

Fig. 4| SARS-2-S syncytium formation triggers the UPR-mediated accumulation of dsRNA that is recognized by RIG-I. a, Confocal microscopic images of MAVS and dsRNA in cocultured A549 cells at 3 hpc. Purple, MitoTracker staining for

mitochondria; green, MAVS staining; red, J2 staining for dsRNA; blue, DAPI staining. A magnified view of the boxed region was also shown. Scale bars represented 10 μm (whole image) and 1 μm (magnified). **b,** Colocalization was quantified by calculating the Manders' colocalization coefficient (MCC) for dsRNA with MAVS or mitochondria. **c,** GSEA of expressed genes related to ER stress-related DEGs in cocultured 293T cells at 2 hpc. NES, normalized enrichment score; RLM, ranked list metric. **d,** Immunofluorescence analysis of XBP-1 splicing in A549 cells cocultured for the indicated times in the presence of DMSO or 4-PBA (5 mM). A549-S and A549-ACE2 cells were transfected with XBP-1-EGFP 24 h before coculture start. Spliced XBP-1 was detected based on the GFP signal. **e,** Confocal microscopic images of MAVS and dsRNA in cocultured A549 cells at 3 hpc in the presence of DMSO or 4-PBA. Purple, MitoTracker staining for mitochondria; green, MAVS staining; red, J2 staining for dsRNA; blue, DAPI staining. Scale bars represented 10 μm. **f,** MAVS aggregation in A549 cells cocultured for the indicated times in the presence of 4-PBA or DMSO. α-tubulin was used as a loading control. **g,** Normalized expression of *CDKN1A*, *TNF*, *IL6*, and *IL8* in cocultured A549 cells at 4 hpc in the presence of DMSO or 4-PBA (5 mM) relative to that at 0 hpc treated with DMSO by RT-qPCR. **h**, MAVS aggregation in siCtrl or siIRE1α cells cocultured for the indicated times. α-tubulin was used as a loading control. All images were representative of three independent experiments. All quantified data were presented as the mean ± SD of n = 3 independent experiments. Statistical significance was determined using two-tailed Student's *t* test (**g**).

Fig. 5

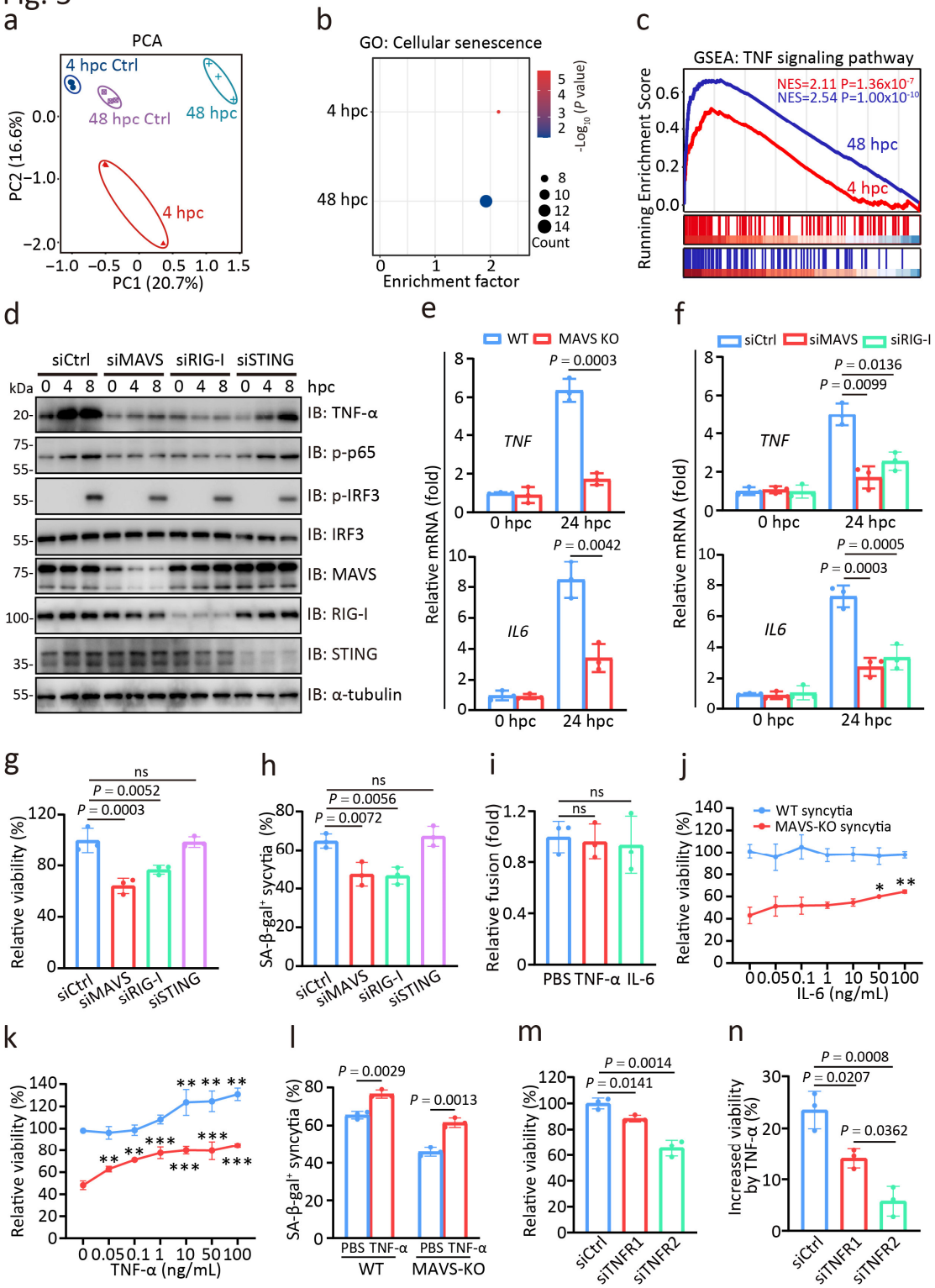

Fig. 5| MAVS–TNF-α signalling regulates the survival to senescence fate of SARS-2-S syncytia. a, PCA of gene expression patterns in A549 cells cocultured for the indicated times. In all plots, each point represented an independent biological replicate.

b, Senescence pathways enriched in the samples analysed in **a**, based on GO term analysis. **c,** GSEA of genes related to TNF signalling pathway among the DEGs in cells from **a**. NES, normalized enrichment score. **d,** Immunoblotting analysis of proteins of activated IFN-I signalling pathway in siCtrl, siMAVS, siRIG-I, or siSTING cells cocultured for the indicated times. All these siRNA oligos were transfected to A549-S and A549-ACE2 cells 24 h before coculture start. α-tubulin used as the loading control. **e,f,** Normalized expression of the *TNF* and *IL6* in WT and MAVS-KO cocultured 293T cells (**e**) or siCtrl, siMAVS, and siRIG-I (**f**) cocultured 293T cells at 24 hpc relative to that at 0 hpc. **g,** Relative cell viability of siMAVS, siRIG-I, or siSTING cocultured cells at 24 hpc by CCK8 assay. Cell viability of siCtrl cocultured cells at 24 hpc was set to 100%. All these siRNA oligos were transfected to A549-S and A549-ACE2 cells 24 h before coculture. **h,** SA-β-gal positivity in cocultured cells from **g**. **i,** Relative fusion of cocultured A549 cells at 24 hpc in the presence of TNF-α (100 ng/mL) or IL-6 (100 ng/mL) by β-galactosidase assay. The fusion level of cocultured A549 cells treated with PBS was set to 1. **j,k,** Relative cell viability of WT or MAVS-KO cocultured cells at 48 hpc in the presence of IL-6 **(j)** or TNF-α **(k)**. Cell viability of WT cocultured cells at 48 hpc was set to 100%. **l,** SA-β-gal positivity in WT or MAVS-KO cocultured cells at 48 hpc in the presence of TNF-α. **m,** Relative cell viability of siTNFR1 or siTNFR2 cocultured A549 cells at 24 hpc. Cell viability of siCtrl cells at 24 hpc was set to 100%. **n**, Increased cell viability of siCtrl, siTNFR1, or siTNFR2 cocultured cells at 48 hpc in the presence of TNF-α than that in the presence of PBS. All quantified data were shown as the mean ± SD of n = 3 independent experiments. Statistical significance was

determined using two-tailed Student's *t* test (**e**), or one-way ANOVA and Bonferroni's post hoc analysis (**f, g, h, i, j, k, l, m, n**).

Fig. 6

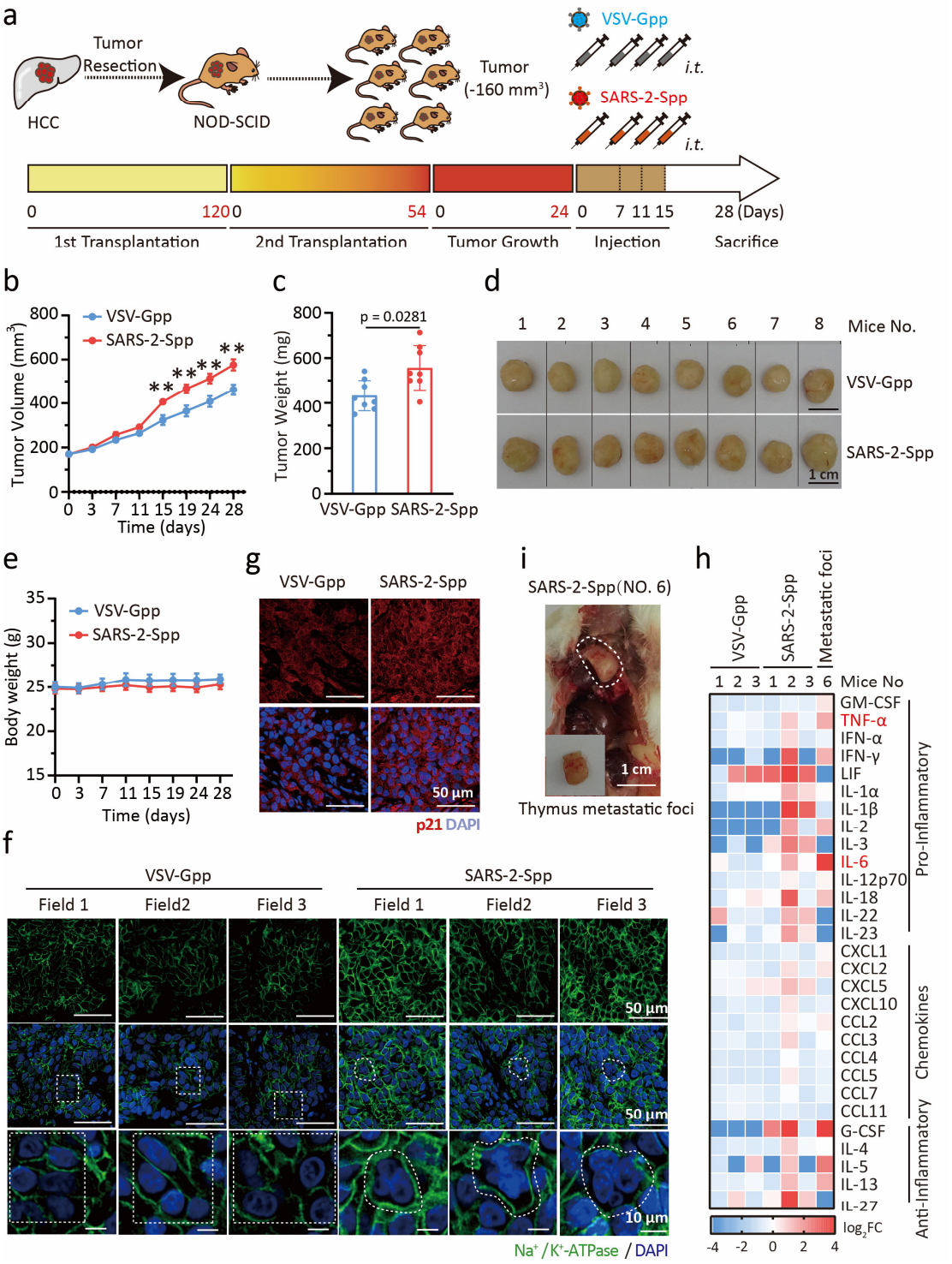

Fig. 6| Massive accumulation of senescent SARS-2-S syncytia exerts a tumour-promoting effect. a, Overview of the PDX mouse model. Cells obtained from resected HCC tissue with strong ACE2 staining were subcutaneously injected into the back of mouse, which was then injected with 50 μL of VSV-Gpp or SARS-2-Spp at a

concentration of 2.6×10^8 TU/mL. **b, c,** PDX tumour volume **(b)** and terminal tumour weight **(c)**. **d,** Images of tumours from PDX mice. **e,** Mice weight over the course of the experiment. **f,** Immunohistochemical analysis of multinucleated cells in tumour tissues from SARS-2-Spp-treated or VSV-Gpp-treated mice. Green, Na^+/Ka^+-ATPase staining for cell membrane; blue, nuclear DAPI staining. Scale bars represented 50 μm or 10 μm as indicated. **h,** Multiplex bead-based proteins analysis in the serum from VSVG-pp-mice, SARS-2-Spp-mice, or SARS-2-Spp-mice with metastasis. **i,** One thymus metastatic foci was noted from SARS-2-S-treated mouse No. 6. All images were representative of three independent experiments. Statistical significance was determined using two-tailed Student's *t* test (**c**) or one-way ANOVA and Bonferroni's post hoc analysis (**b**).

Extended Data Figures and Extended Data Figure legends

Extended Data Fig. 1

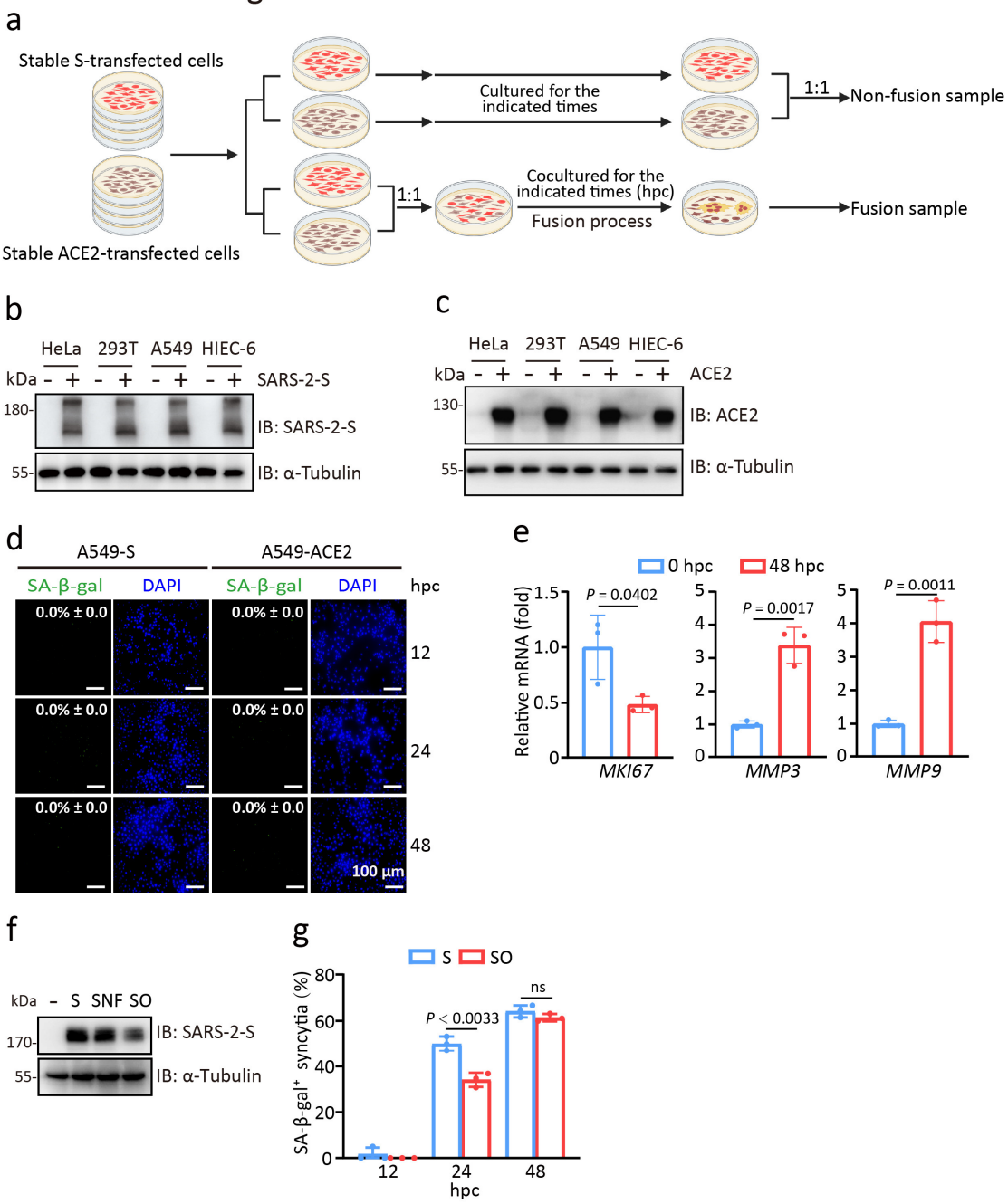

Extended Data Fig. 1| SARS-2-S syncytia exhibit a senescence-like phenotype. a, Illustration of the cell coculture system. Cells were stably transfected with plasmid DNA expression of S or human ACE2, which was followed by cocultured at 1:1 ratio for the indicated times. A mixture of A549-S cells and A549-ACE2 cells mixed at 1:1 ratio without coculture (0 hpc) was used as a non-fusion control. **b-c,** Immunoblot

analysis of S (b) and ACE2 (c) expression in A549, 293T, HeLa, and HIEC-6 cells transfected with the indicated plasmids. α-Tubulin was used as a loading control. **d,** SA-β-gal staining of A549-S or A549-ACE2 cells. Green, SA-β-gal staining; blue, nuclear DAPI staining. Scale bars represented 100 μm. **e,** Relative expression of *MKI67*, *MMP9*, and *MMP3* in cocultured A549 cells at 48 hpc compared to that at 0 hpc by RT-qPCR. **f,** Immunoblot analysis of A549 cells transfected with S, SNF, or SO. α-Tubulin was used as a loading control. **g,** Quantification of SA-β-gal-positivity in S- or SO-transfected A549 and A549-ACE2 cells cocultured for the indicated hpc. Scale bars represented 100 μm. All images were representative of three independent experiments. Statistical significance was determined with two-tailed Student's t test (e, g).

Extended Data Fig. 2

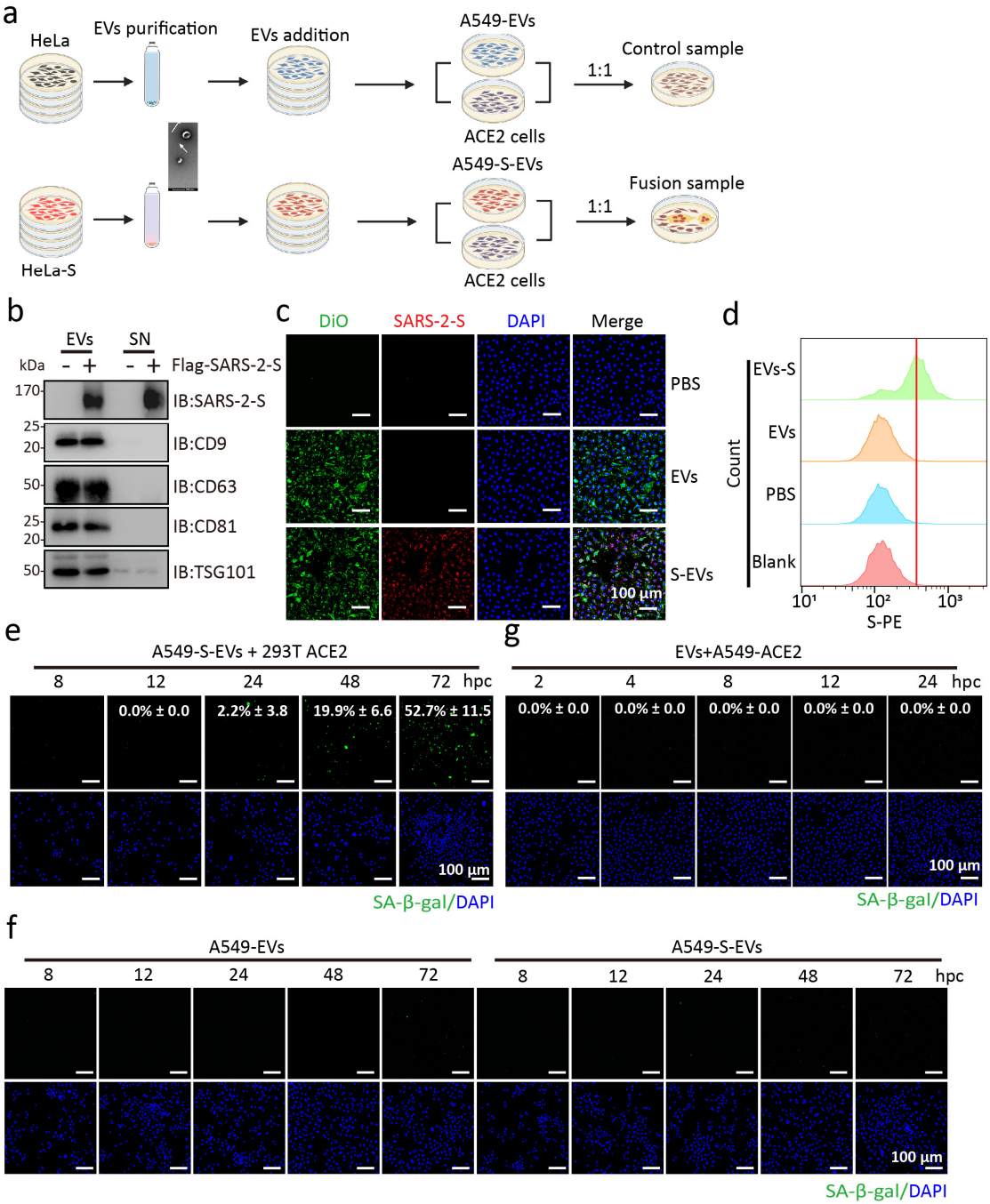

Extended Data Fig. 2| SARS-2-S delivered by EVs triggers syncytial senescence. a, Illustration of EVs-mediated FFWI. Cells were treated with S-EVs for 24 h, followed by coculture with ACE2-expressing cells for the indicated times. A mixture of A549-EVs and A549-ACE2 cells was used as a non-fusion control. **b,** Immunoblot analysis of EVs markers (CD9, CD63, CD81, and TSG101) and S expression in EVs purified

from the supernatant (SN) of HeLa or HeLa-S. **c,** Analysis of DiO-labelled S-EVs or EVs uptake by A549 cells. Green, DiO-labelled EVs; red, S staining; blue, nuclei DAPI staining. **d,** Flow cytometry analysis of S expression on the cell surface of A549-S-EVs cells. **e, g,** SA-β-gal staining of A549-S-EVs cells cocultured with 293T-ACE2 cells (e) or EVs-treated A549-ACE2 (g) for the indicated times. Green, SA-β-gal staining; blue, nuclei DAPI staining. Scale bars represented 100 μm. **f,** SA-β-gal staining of EVs- or S-EVs-treated A549 cells for the indicated times. Green, SA-β-gal staining; blue, nuclei DAPI staining. Scale bars represented 100 μm. All the images were representative of three independent experiments.

Extended Data Fig. 3

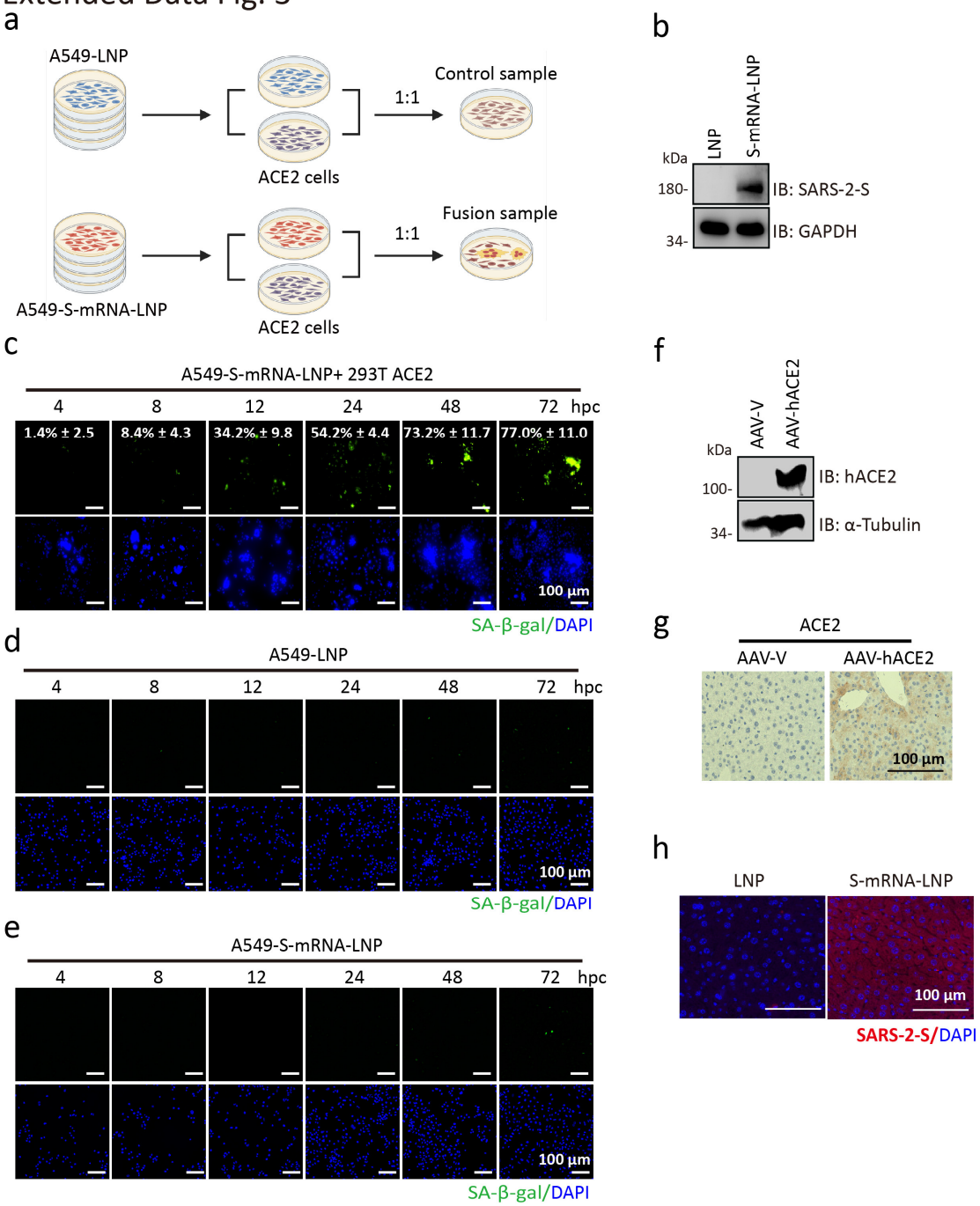

Extended Data Fig. 3|SARS-2-S delivered by mRNAs triggers syncytial senescence. **a,** Illustration of the cell coculture system mediated by S-mRNAs. Cells were treated with S-mRNA-LNP for 24 h, which was followed by coculture with ACE2-expressing cells for the indicated times. A mixture of A549-LNP and A549-ACE2 cells was used as non-fusion control. **b,** Immunoblot analysis of S expression in A549 cells treated

with S-mRNA-LNP. GAPDH was used as a loading control. **c,** SA-β-gal staining of A549-S-mRNA-LNP cells cocultured with 293T-ACE2 cells for the indicated times. Green, SA-β-gal staining; blue, nuclei DAPI staining. Scale bars represented 100 μm. **d,e,** SA-β-gal staining of LNP- **(d)** or S-mRNA-LNP-treated **(e)** A549 cells cultured for the indicated times. Green, SA-β-gal staining; blue, nuclei DAPI staining. Scale bars represented 100 μm. **f,g,** ACE2 expression in livers from mice injected with S-mRNA-LNP or LNP by immunoblotting **(f)** or immunohistochemical staining **(g)**. All the images were representative of three independent experiments.

Extended Data Fig. 4

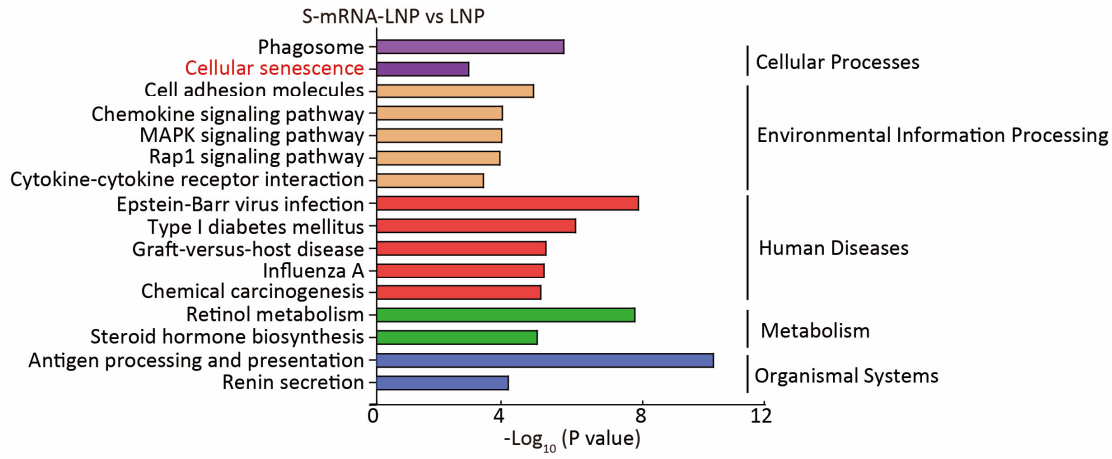

Extended Data Fig. 4|SARS-2-S delivered by mRNAs triggers syncytial senescence. Pathways enriched in DEGs identified in the livers of mice injected with LNP or S-mRNA-LNP according to KEGG functional pathways at level 1. The bar plot shows significantly dysregulated pathways ($P < 0.05$), with Fisher's exact test P-values shown on the x-axis.

Extended Data Fig. 5

a

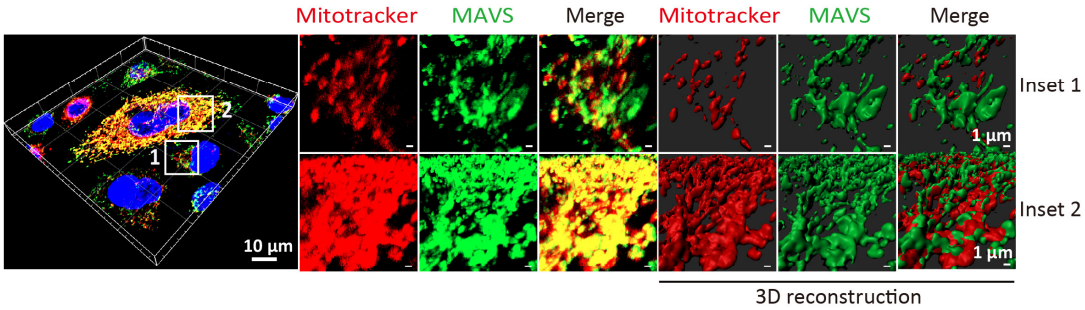

b

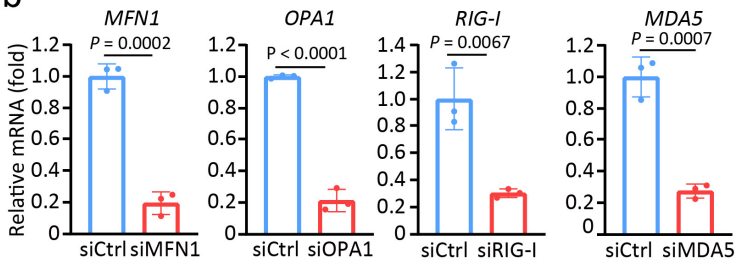

c

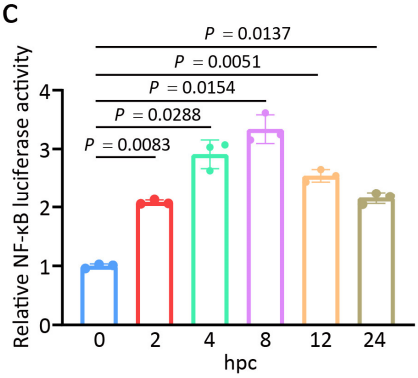

Extended Data Fig. 5| SARS-2-S syncytia induce the formation of functional MAVS aggregates dependent on RIG-I. a, Confocal microscopic images of MAVS and mitochondria in cocultured A549 cells at 4 hpc. Red, MitoTracker staining for mitochondria; green, MAVS staining; blue, DAPI staining. A magnified view of the boxed region was shown in the middle panel, and a 3D reconstruction of the Z stacks was shown in the right panel. Scale bars represented 10 µm (whole image) and 1 µm (magnified). **b,** Knockdown efficiency of siMAVS, siRIG-I, siMFN1, or siOPA1 compared to siCtrl by RT-qPCR. **c,** Relative luciferase activity of NF-κB in cocultured A549 cells for the indicated times. Luciferase activity was normalized to the values of

0 hpc. All quantified data in this figure were shown as the means ± SDs of n = 3 independent experiments. Statistical significance was determined with two-tailed Student's t test (b), one-way ANOVA and Bonferroni's post hoc analysis (c).

Extended Data Fig. 6

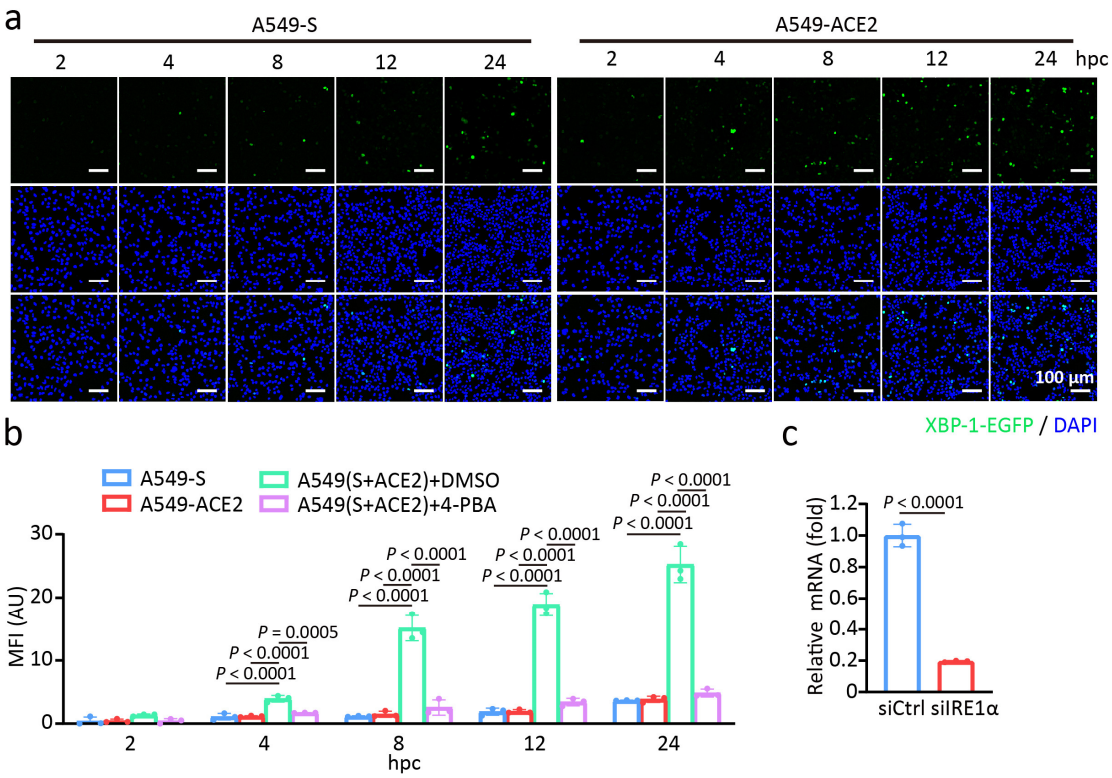

Extended Data Fig. 6| SARS-2-S syncytium formation triggers the UPR-mediated accumulation of dsRNA recognized by RIG-I. a, Immunofluorescence analysis of XBP-1 splicing in A549-S or A549-ACE2 cells transfected with XBP-1-EGFP for the indicated times. Spliced XBP-1 is indicated by the GFP signal. **b,** Quantification of the mean fluorescence intensity (MFI) in A549-S, A549-ACE2, and cocultured A549 cells in the presence of DMSO or 4-PBA for the indicated times. **c,** Knockdown efficiency of siIRE1α compared to siCtrl by RT-qPCR. All the images were representative of three independent experiments. All quantified data in this figure were shown as the means ± SDs of n = 3 independent experiments. Statistical significance was determined with one-way ANOVA and Bonferroni's post hoc analysis (b), two-tailed Student's t test (c).

Extended Data Fig. 7

a

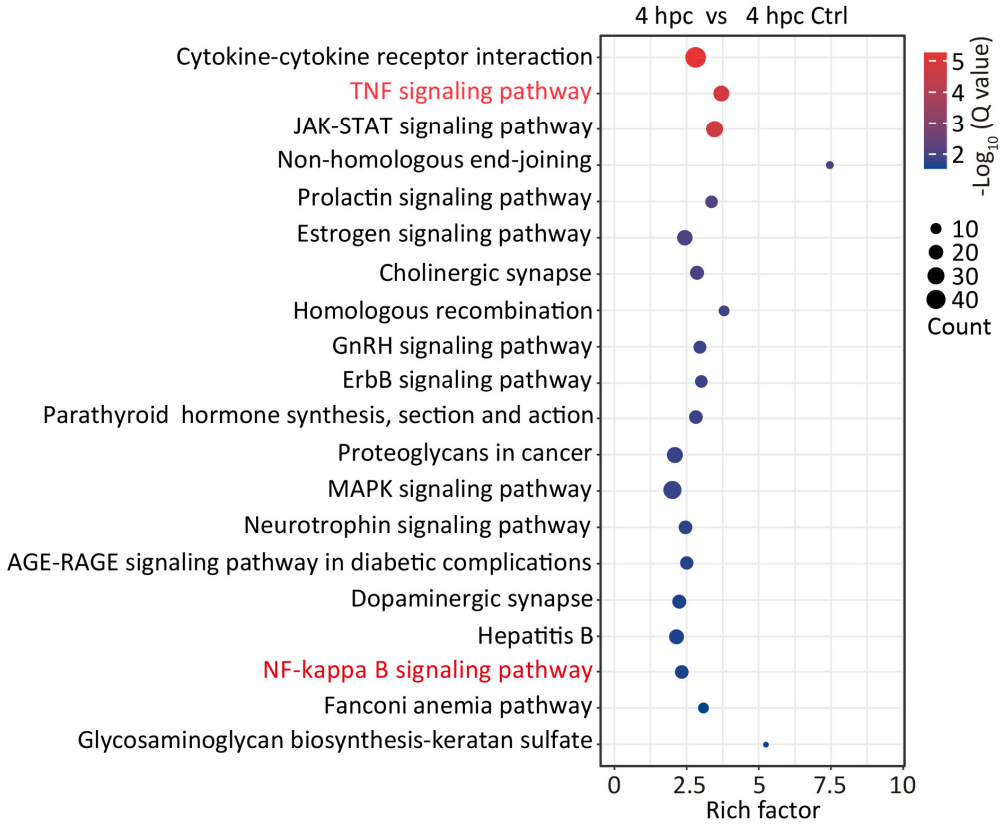

b

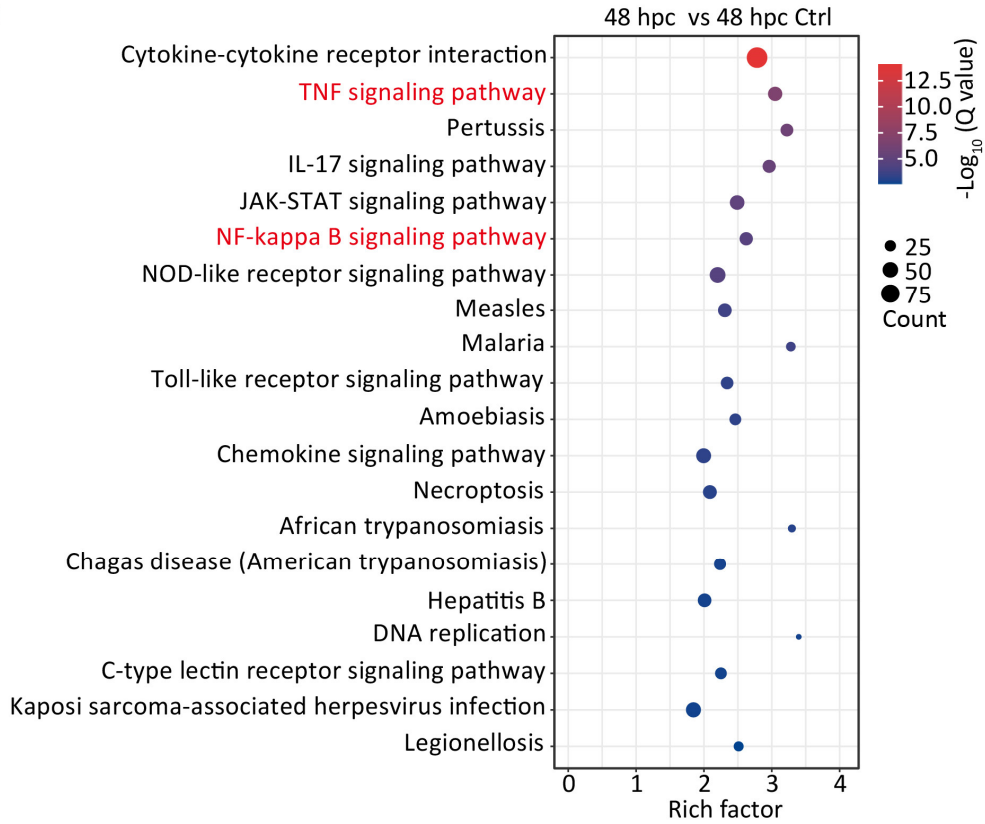

Extended Data Fig. 7| MAVS-TNF-α regulates the survival to senescence of SARS-2-S syncytia. a,b, Twenty most significantly enriched pathways in cocultured A549 cells at 4 hpc **(a)** and 48 hpc **(b)** according to KEGG pathway analysis. The enriched terms are shown on the y-axis and the P-values (log transformed) assessing significant enrichment are shown on the x-axis with Fisher's exact test. The enrichment degree of KEGG is measured by enrichment factors (Rich factor), P-value and the number of genes count enriched in this pathway.

Extended Data Fig. 8

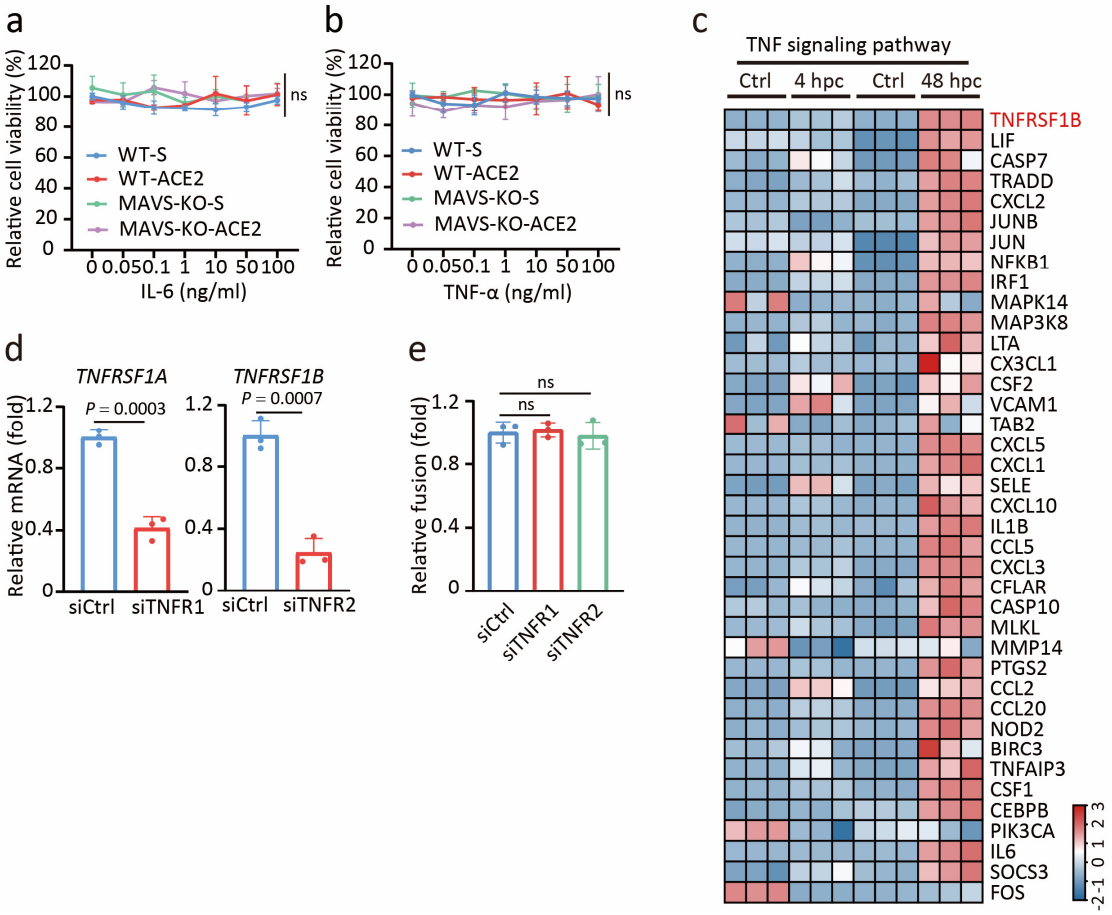

Extended Data Fig. 8| MAVS-TNF-α regulates the survival of SARS-2-S syncytia. **a,b,** Relative cell viability of WT-S, WT-ACE2, MAVS-KO-S, and MAVS-KO-ACE2 cells treated with IL-6 **(a)** or TNF-α **(b)** at the indicated concentrations. Cell viability of cells treated with PBS was set to 100%. **c,** Heatmap of the critical DEGs of the TNF signalling pathway in cocultured A549 cells at 4 hpc and 48 hpc. **d,** Knockdown efficiency of siTNFRSF1A or siTNFRSF1B compared to siCtrl by RT-qPCR. **e,** Relative fusion of siTNFR1 and siTNFR2 cocultured A549 cells at 24 hpc by β-galactosidase assay. The fusion level of siCtrl cocultured cells at 24 hpc was set to 1. All quantified data were shown as the means ± SDs of n = 3 independent experiments. Statistical significance was determined with two-tailed Student's t test (d), one-way

ANOVA and Bonferroni's post hoc analysis (a, b, e).

Extended Data Fig. 9

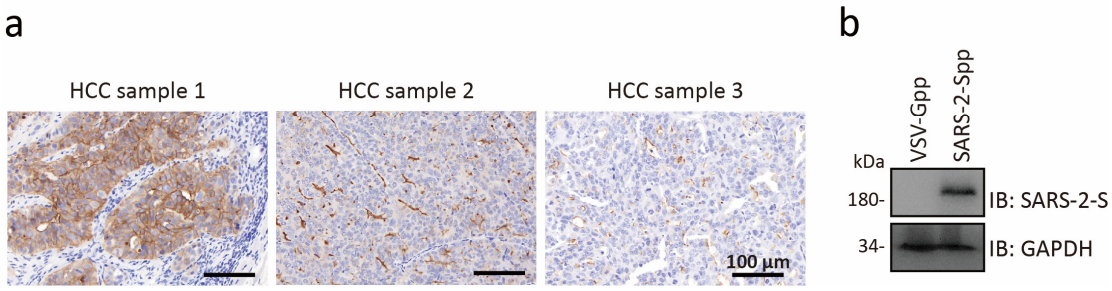

Extended Data Fig. 9| Massive accumulation of senescent SARS-2-S syncytia exerts a tumour-promoting effect. a, Immunohistochemical analysis of resected three HCC samples with anti-ACE2 antibodies. **b,** Immunoblot analysis of SARS-2-S expression in A549 cells with VSVG-pp or SARS-2-Spp for 24 h by anti-SARS2-S antibody. GAPDH was used as a loading control.

Extended Data Fig. 10

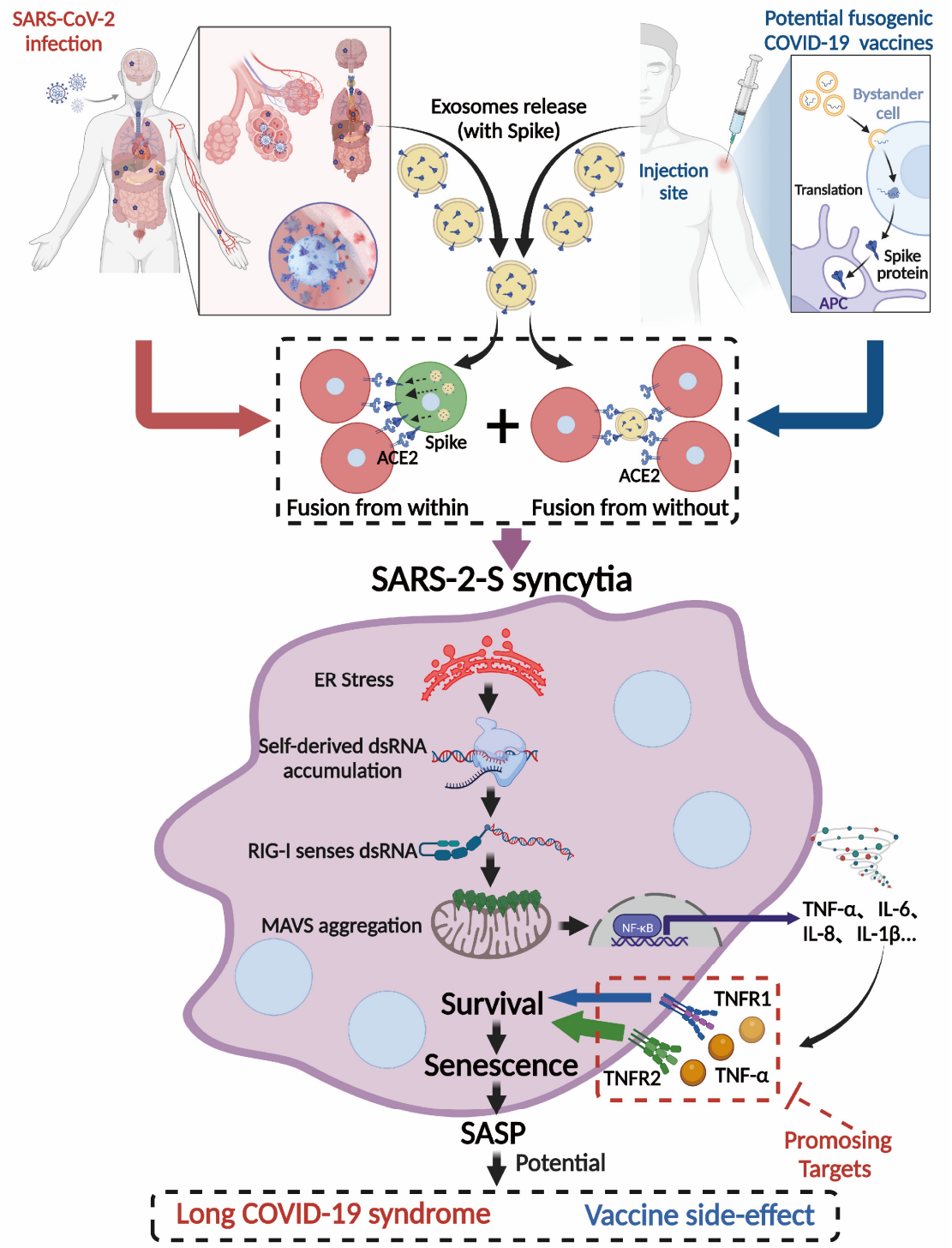

Extended Data Fig. 10| Innate immune sensing of self-derived double-stranded RNA by RIG-I-MAVS-TNF-α regulates the survival and senescence fate of SARS-2-S syncytia. SARS-2-S induced syncytia via FFWI and FFWO manner exhibits a senescence-like phenotype regardless of the cell type or syncytium nucleus number.

Mechanistically, ER stress triggered by SARS-2-S syncytia generates self-derived dsRNA that activates the cytosolic RNA-sensing RIG-I-MAVS pathway to drive the TNF-α-dependent survival and senescence fate of SARS-2-S syncytia. As the main surface-exposed antigen with high fusogenic efficiency and persistence existence, SARS-2-S might contribute to the side effects of particular COVID-19 vaccines or perhaps long COVID-19 syndrome and that induction of syncytium death by targeting TNF-α may be an effective intervention strategy.

Supplementary Information

Table S1. siRNA sequences

Gene	Sense (5'-3')	Antisense (5'-3')
TNF	GCCUGUAGCCCAUGUUGUATT	UACAACAUGGGCUACAGGCTT
TNFRSF1A	GGUCAGGUGGAGAUCUCUUTT	AAGAGAUCUCCACCUGACCTT
TNFRSF1B	CCGGCUCAGAGAAUACUAUTT	AUAGUAUUCUCUGAGCCGGTT
IRE1α	CCUUUCUCCCAGAUCCUAATT	UUAGGAUCUGGGAGAAAGGTT
RIG-I	GCCAGAAUCUUAGUGAGAATT	UUCUCACUAAGAUUCUGGCTT
STING	CCGGAUUCGAACUUACAAUTT	AUUGUAAGUUCGAAUCCGGTT
MAVS	CUGCCGCAAUUUCAGCAAUTT	AUUGCUGAAAUUGCGGCAGTT
MDA5	CCAACUGCUGAACCUCCUUTT	AAGGAGGUUCAGCAGUUGGTT
MFN1	CCUAGAUGCUGAUGUCUUUTT	AAAGACAUCAGCAUCUAGGTT
OPA1	GCCUGACAUUGUGUGGGAATT	UUCCCACACAAUGUCAGGCTT

Table S2. Primer sequences

Gene	Forward (5'-3')	Reverse (5'-3')
CDKN1A	ATGAGTTGGGAGGAGGCA	CTGAGCGAGGCACAAGG
MKI67	TATGCCTGTGGAGTGGAAT	GGGTGAGAAAAGGTGCTG
IL6	CCACTCACCTCTTCAGAACG	CATCTTTGGAAGGTTCAGGTTG
IL8	ATACTCCAAACCTTTCCACCC	TCTGCACCCAGTTTTCCTTG
MDA5	GCTGAAGTAGGAGTCAAAGCCC	CCACTGTGGTAGCGATAAGCAG
MFN1	GGTGAATGAGCGGCTTTCCAAG	TCCTCCACCAAGAAATGCAGGC
OPA1	GTGGTTGGAGATCAGAGTGCTG	GAGGACCTTCACTCAGAGTCAC
IRE1α	CCGAACGTGATCCGCTACTTCT	CGCAAAGTCCTTCTGCTCCACA
MMP3	TTTTCTCCTGCCTGTGCT	TTCACGCTCAAGTTCCCT
MMP9	ACGCAGACATCGTCATCC	CCAGGGACCACAACTCG
ACTB	TCTCCCAAGTCCACACAGG	GGCACGAAGGCTCATCA
TNF	ACTTTGGAGTGATCGGCC	GCTTGAGGGTTTGCTACAAC
TNFRSF1A	TGCCAGGAGAAACAGAACAC	TCCTCAGTGCCCTTAACATTC
TNFRSF1B	GTCCACACGATCCCAACAC	TGTCACACCCACAATCAGTC
STING	TCAAGGATCGGGTTTACAGC	GCTTGACTGTATTGTGACATGG
MAVS	ATGGTGCTCACCAAGGTGTCTG	TCTCAGAGCTGCTGTCTAGCCA
RIG-I	CACCTCAGTTGCTGATGAAGGC	GTCAGAAGGAAGCACTTGCTACC